Monthly Notices
of the
ROYAL ASTRONOMICAL SOCIETY

MNRAS **491,** 2939–2952 (2020)
Advance Access publication 2019 November 13

doi:10.1093/mnras/stz3124

Feedback from supermassive black holes transforms centrals into passive galaxies by ejecting circumgalactic gas

Benjamin D. Oppenheimer,[1,2★] Jonathan J. Davies,[3] Robert A. Crain,[3] Nastasha A. Wijers,[4] Joop Schaye,[4] Jessica K. Werk,[5] Joseph N. Burchett,[6] James W. Trayford[4] and Ryan Horton[1]

[1]*CASA, Department of Astrophysical and Planetary Sciences, University of Colorado, 389 UCB, Boulder, CO 80309, USA*
[2]*Harvard-Smithsonian Center for Astrophysics, 60 Garden St., Cambridge, MA 02138, USA*
[3]*Astrophysics Research Institute, Liverpool John Moores University, 146 Brownlow Hill, Liverpool, L3 5RF, UK*
[4]*Leiden Observatory, Leiden University, PO Box 9513, NL-2300 RA, Leiden, the Netherlands*
[5]*Department of Astronomy, University of Washington, Seattle, WA 98195, USA*
[6]*University of California - Santa Cruz, 1156 High Street, Santa Cruz, CA 95064, USA*

Accepted 2019 November 4. Received 2019 November 4; in original form 2019 April 11

ABSTRACT

Davies et al. established that for L^* galaxies the fraction of baryons in the circumgalactic medium (CGM) is inversely correlated with the mass of their central supermassive black holes (BHs) in the EAGLE hydrodynamic simulation. The interpretation is that, over time, a more massive BH has provided more energy to transport baryons beyond the virial radius, which additionally reduces gas accretion and star formation. We continue this research by focusing on the relationship between the (1) BH masses ($M_{\rm BH}$), (2) physical and observational properties of the CGM, and (3) galaxy colours for Milky Way-mass systems. The ratio of the cumulative BH feedback energy over the gaseous halo binding energy is a strong predictor of the CGM gas content, with BHs injecting significantly higher than the binding energy resulting in gas-poor haloes. Observable tracers of the CGM, including C IV, O VI, and H I absorption line measurements, are found to be effective tracers of the total $z \sim 0$ CGM halo mass. We use high-cadence simulation outputs to demonstrate that BH feedback pushes baryons beyond the virial radius within 100 Myr time-scales, but that CGM metal tracers take longer (0.5–2.5 Gyr) to respond. Secular evolution of galaxies results in blue, star-forming or red, passive populations depending on the cumulative feedback from BHs. The reddest quartile of galaxies with $M_* = 10^{10.2-10.7}\,{\rm M}_\odot$ (median $u - r = 2.28$) has a CGM mass that is 2.5 times lower than the bluest quartile ($u - r = 1.59$). We propose observing strategies to indirectly ascertain $f_{\rm CGM}$ via metal lines around galaxies with measured $M_{\rm BH}$. We predict statistically detectable declines in C IV and O VI covering fractions with increasing $M_{\rm BH}$ for central galaxies with $M_* = 10^{10.2-10.7}{\rm M}_\odot$.

Key words: hydrodynamics – methods: numerical – galaxies: formation – quasars: absorption lines – (galaxies:) quasars: supermassive black holes – cosmology: theory.

1 INTRODUCTION

Galaxies residing in Milky Way (MW)-mass haloes display great diversity. While the typical halo mass of $1{-}2 \times 10^{12}\,{\rm M}_\odot$ hosts a central galaxy with a stellar mass of several times $10^{10}\,{\rm M}_\odot$ (e.g. Behroozi, Wechsler & Conroy 2013; Moster, Naab & White 2013), the rate of present-day star formation (SF) varies by orders of magnitude (e.g. Somerville et al. 2008; Moustakas et al. 2013; Henriques et al. 2015). This is often discussed in terms of the 'blue' SF cloud and the 'red' passive sequence, and appears to indicate a process of galaxy transformation sometimes referred to as 'quenching'. Revealing the process by which a galaxy's star formation rate (SFR) is curtailed over a relatively narrow range of halo mass is a key motivation for exploring sophisticated models of galaxy formation and evolution, especially cosmologically based hydrodynamic simulations that self-consistently follow the gas that fuels SF.

Cosmological hydrodynamic simulations that are now able to reproduce fundamental properties of galaxy populations and the morphological sequence of the Hubble Tuning Fork include EAGLE (Evolution and Assembly of GaLaxies and their Environments;

★ E-mail: benjamin.oppenheimer@colorado.edu

Schaye et al. 2015), Illustris-TNG (Pillepich et al. 2018), Horizon-AGN (Dubois et al. 2016), and MUFASA (Davé, Thompson & Hopkins 2016), the first of which we use here. Galaxy formation theory has long predicted a transition at the $\sim 10^{12}\,\mathrm{M}_{\odot}$ dark matter (DM) halo mass above which virial equilibrium achieves temperatures with lowered baryonic cooling efficiencies (Rees & Ostriker 1977; Silk 1977; White & Rees 1978). Nevertheless, the cooling rate in gaseous haloes, now termed the circumgalactic medium (CGM), is overefficient in forming stars compared to the stellar fraction observed in galaxies (White & Frenk 1991; Balogh et al. 2001; Kereš et al. 2005). Simulations apply feedback mechanisms to reduce the efficiency of accretion on to and star formation within a galaxy to solve this overcooling problem. Earlier hydrodynamic models applied forms of stellar superwind feedback to eject baryons from the galactic sites of star formation to overcome this overcooling problem (Springel & Hernquist 2003; Oppenheimer & Davé 2006; Schaye et al. 2010). While these simulations often reproduced lower mass galaxy properties, their lack of feedback from supermassive black hole (BH) growth was considered a possible missing ingredient for preventing continued star formation and stellar assembly in galaxies at and above MW masses (e.g. Oppenheimer et al. 2010).

Since its earliest inclusions in cosmological models, BH feedback is required to become effective at the MW-mass scale to reproduce galaxy properties (e.g. Bower et al. 2006; Croton et al. 2006; Sijacki et al. 2007; Booth & Schaye 2009). Hence, the halo mass at which cooling efficiencies decline is similar to the masses where significant BH feedback turns on. This may not be a coincidence as argued by Bower et al. (2017), who link the rapid phase of BH growth to the formation of a hot halo that prevents efficient ejective stellar feedback. Using the same EAGLE simulation we explore here, Bower et al. (2017) showed that buoyant thermal stellar feedback becomes inefficient upon the formation of a hot halo at halo mass $\sim 10^{12}\,\mathrm{M}_{\odot}$, concentrating gas in the centre, where it triggers non-linear BH growth and feedback. The BH feedback imparted to the surrounding halo effectively curtails star formation and can transition the galaxy from the blue cloud to the red sequence.

As already discussed, the central galaxies hosted by MW-mass haloes have diverse SFRs, colours, morphologies, and BH masses, M_{BH}. Davies et al. (2019a, hereafter D19) used EAGLE to show that the diversity extends to their gaseous haloes with the primary astrophysical driver being M_{BH}, which can be thought of as proportional to the integral of BH feedback energy imparted over its growth history. The rapid BH growth phase during which M_{BH} multiplies by factors of several over a small fraction of the Hubble time-scale also clears out a significant fraction of the baryons in the CGM. D19 demonstrated that the gaseous baryon fraction, f_{CGM}, at a given halo mass is highly anticorrelated with M_{BH}, indicating a causal relation between f_{CGM} and M_{BH}. This conclusion was confirmed by comparing to a simulation without AGN feedback. They also showed that the greatest scatter of f_{CGM} in EAGLE occurs at halo masses $M_{200} = 10^{12.0-12.3}\,\mathrm{M}_{\odot}$, where M_{200} is the mass within a sphere within which the mean internal density is 200 times the critical overdensity. Following D19, we define

$$f_{\mathrm{CGM}} \equiv M_{\mathrm{gas}}(R < R_{200})/M_{200}(R < R_{200}) \times \Omega_{\mathrm{M}}/\Omega_{\mathrm{b}}, \qquad (1)$$

where R_{200} indicates the radius of a spherical M_{200} mass distribution. Here, M_{gas} includes all CGM gas regardless of temperature, but excludes ISM gas, defined as gas particles with non-zero SFR, which is in contrast with D19 and leads to only a small decrease. D19 also showed that f_{CGM} is highly correlated with SFR, which they argue is a result of the BH removing CGM gas that provides fuel for further SF. Furthermore, Davies et al. (2019b) demonstrated this behaviour is not unique to only EAGLE as the Illustris-TNG simulation also shows a causal relationship between f_{CGM} and SFR owing to BH feedback. They further show both simulations have significant correlations between more rotationally supported morphologies and f_{CGM}.

f_{CGM} is not directly obtainable for galactic haloes with current observational facilities. While D19 determined that soft X-ray emission and thermal Sunyaev–Zel'dovich (S–Z) measurements serve as effective indicators of the baryon fraction within haloes, X-ray (e.g. Bogdán et al. 2013; Li et al. 2017), and S-Z (Planck Collaboration XI 2013; Greco et al. 2015) measurements for a statistically significant sample of MW-mass galaxies are beyond the capabilities of current instrumentation. In contrast, the UV probes of the CGM afforded by the Cosmic Origins Spectrograph (COS) on the *Hubble Space Telescope* provide a growing data base of gaseous halo measurements that can be correlated with galaxy properties (e.g. Stocke et al. 2013; Tumlinson et al. 2013; Burchett et al. 2015; Tumlinson, Peeples & Werk 2017). Studies that combine gas column density measurements from UV absorption-line spectra with ionization modelling have estimated f_{CGM} for galaxies with $\mathrm{M}_{200} \approx 10^{12}\,\mathrm{M}_{\odot}$ to range from 25–100 per cent, albeit subject to large systematic uncertainties (e.g. Werk et al. 2014; Prochaska et al. 2017). One goal is to develop a strategy to observe an empirical indicator of the baryonic content of gaseous haloes around nearby galaxies, for which we can also obtain an estimate of M_{BH}.

D19 demonstrated that it is the integral of BH feedback, not the instantaneous BH feedback, that ultimately ejects baryons beyond R_{200}. Specifically, while f_{CGM} strongly anticorrelates with M_{BH}, it does not correlate at a significant level with the BH accretion rate at $z = 0$. This is supported by the observational result that COS sightlines intersecting haloes hosting low-redshift AGN show little, if any, effect on CGM ion column densities (Berg et al. 2018).

Another of our goals is to explore the relations and time-scales between BH feedback and the clearing of the gas from the CGM. We leverage high-cadence EAGLE 'snipshot' outputs that track galaxies, BHs, and CGM absorption signatures on $\lesssim 100$ Myr time-scales. Correa, Schaye & Trayford (2019) used the same snipshots to determine a causal link between AGN activity and the transition of a central galaxy's colour from the blue cloud into the 'green valley' of intermediate galaxy colours, and to the red sequence (see also Trayford et al. 2016). We extend this type of investigation to the CGM to determine how rapidly baryons within R_{200} respond, as well as UV absorption line indicators of f_{CGM}.

The final goal of this study is to connect the baryonic content of the CGM to the processes by which a galaxy becomes a part of the red sequence or remains in the blue cloud. From the strong correlation between f_{CGM} and galactic SFR (D19; Davies et al. 2019b), we expect a galaxy's colour to also change in response to the BH. Therefore, we use the SKIRT radiative transfer scheme (Camps & Baes 2015) that applies dust-reddening to EAGLE galaxies (Trayford et al. 2017) to consider the following questions: Can rapid BH growth not only lift the CGM, but change the colour of a galaxy by curtailing the fuel supply for SF? Is the CGM of a red galaxy substantially more diffuse and less massive than that of a blue galaxy in the MW halo mass range? What is the relationship between a galaxy's colour, its CGM content probed in the UV, and its central BH?

The paper is laid out as follows. We introduce the EAGLE simulation, define our galaxy samples, and describe the methods to calculate physical and observational quantities in Section 2. In Section 3, we revisit the work of D19 linking the CGM gas fraction to $M_{\rm BH}$ and introduce the ratio of BH feedback energy relative to the binding energy of the CGM. We then discuss available UV indicators for $f_{\rm CGM}$, highlighting C IV covering fractions, around galaxies in the local Universe in Section 4. We access high-cadence outputs to track the CGM in response to the central BH in Section 5 and integrate galaxy colours into the analysis in Section 6. We discuss how the O VI ion traces the CGM baryon content in Section 7.1, how the efficiency of BH feedback determines galaxy properties in Section 7.2, and consider our Galaxy's BH and CGM in Section 7.3. We summarize in Section 8.

2 SIMULATIONS

2.1 The EAGLE simulation and black hole energetics

We use the main EAGLE 'Reference' simulation volume that is 100 comoving Mpc on a side, referred to as Ref-L100N1504. This 1504^3 DM and smooth particle hydrodynamic (SPH) particle run uses a heavily modified version of the *N*-body or Hydrodynamical code GADGET-3 (last described in Springel 2005). The DM particle masses are $9.7 \times 10^6\,{\rm M}_\odot$ and the initial SPH particle masses are $1.8 \times 10^6\,{\rm M}_\odot$. The simulation was originally published by Schaye et al. (2015) and Crain et al. (2015; see McAlpine et al. 2016; Camps et al. 2018, for the public release). EAGLE applies the pressure-entropy SPH formulation of Hopkins (2013) with a series of additional SPH implementations referred to as ANARCHY (see Appendix A of Schaye et al. 2015). EAGLE assumes a Planck Collaboration XI (2013) cosmology ($\Omega_{\rm m} = 0.307$, $\Omega_\Lambda = 0.693$, $\Omega_{\rm b} = 0.04825$, $H_0 = 67.77\,{\rm km\,s^{-1}\,Mpc^{-1}}$).

The EAGLE code applies a number of subgrid physics modules, which include radiative cooling (Wiersma, Schaye & Smith 2009a), star formation (Schaye & Dalla Vecchia 2008), stellar evolution and metal enrichment (Wiersma et al. 2009b), BH formation and accretion (Booth & Schaye 2009; Rosas-Guevara et al. 2015; Schaye et al. 2015), stellar feedback (Dalla Vecchia & Schaye 2012), and BH feedback (Booth & Schaye 2009). The stellar and BH feedback schemes both use thermal prescriptions, where the imparted feedback energy heats local SPH particles. The calibration of these schemes is described in Crain et al. (2015).

The BH (AGN) feedback scheme is critically important for our calculations of BH feedback energy. As in Springel, Di Matteo & Hernquist (2005), EAGLE follows BHs from seed particles that have an initial mass of $10^5\,h^{-1}\,{\rm M}_\odot$, where $h = 0.6777$. BH seeds are placed at the centre of every halo that exceeds $10^{10}\,h^{-1}\,{\rm M}_\odot$. As described in Schaye et al. (2015), BH particles grow both by mergers with other BH particles and through gas accretion. The growth rate of a BH due to gas accretion is $\dot{m}_{BH} = (1 - \epsilon_r)\dot{m}_{\rm acc}$, where $\dot{m}_{\rm acc}$ is the gas accretion rate based on the Bondi & Hoyle (1944) rate and ϵ_r, the radiative efficiency of the accretion disc, is assumed to be 10 per cent. The energy feedback rate imparted to the surrounding gas particles is $\epsilon_f \epsilon_r \dot{m}_{\rm acc} c^2$, where the thermal feedback efficiency $\epsilon_f = 15$ per cent (the other 85 per cent is assumed to be radiated away with no coupling to the surrounding gas). Hence, we calculate a BH energy feedback efficiency based on the BH mass using

$$E_{\rm BH} = \frac{\epsilon_f \epsilon_r}{1 - \epsilon_r} M_{\rm BH} c^2, \tag{2}$$

which translates to 1.67 per cent of the rest mass of the BH with c being the speed of light. Although seed particles do not contribute to the feedback energy in the above equation, their contributions to the mass assembly are small (e.g. Booth & Schaye 2009), since the final mass of BHs in MW mass galaxies by $z = 0$ is typically $\gg 10^5\,h^{-1}\,{\rm M}_\odot$. We finally note that this BH model is highly successful at reproducing the observed soft and hard X-ray luminosity functions of AGN (Rosas-Guevara et al. 2016), and the only main discrepancy is an underestimation of luminous AGN at high redshift, which predominantly reside at mass scales above our focused halo mass range.

2.2 Central galaxy samples

We focus on a subset of MW-mass central galaxies. Our main sample is referred to as the 'M^*' sample, which has $M_* = 10^{10.2-10.7}\,{\rm M}_\odot$ in haloes with $M_{200} = 10^{12.0-12.3}\,{\rm M}_\odot$ and contains 514 galaxies in the 10^6 comoving Mpc^3 volume. These objects show great diversity in $f_{\rm CGM}$, $M_{\rm BH}$, and SFR (D19, their fig. 2). We also consider all central galaxies that have $M_* = 10^{10.2-10.7}\,{\rm M}_\odot$ regardless of M_{200} in the 'L^*' sample, containing 1106 galaxies, because an observational determination of M_{200} is often unavailable. We will show that this sample, which additionally contains 342 (250) galaxies with $M_{200} < 10^{12.0}$ ($>10^{12.3}$) ${\rm M}_\odot$, often produces similar trends as the M^* sample.

Finally, we identify a sample of secularly evolving M^* galaxies that have not experienced a major merger since at least $z = 1.487$, according to the EAGLE merger trees calculated from the 13 snapshots between $z = 1.487$ and 0.0. A major merger is defined as at least a 3:1 ratio merger with another galaxy of at least $M_* = 10^{9.5}\,{\rm M}_\odot$. This 'secular' sample contains 246 galaxies. While this sample represents a biased sample of M^* galaxies, these galaxies are used for high-cadence tracking with up to 155 'snipshot' outputs going back to $z = 5$ to capture the influence of the black hole on the galaxy and its CGM. This work is similar to Correa et al. (2019), who used snipshot outputs to determine the time-scale of galaxy transformation to the red sequence, but our investigation focuses on our refined subset of galaxies and considers their CGM properties. While mergers provide a mechanism for galaxy transformation, our focus is on how central black holes impact galaxies through feedback injected into the CGM.

2.3 Descriptions of physical and observational quantities

2.3.1 *Black hole masses*

We report BH masses as that of the most massive BH within 50 kpc of the galaxy centre. Other black holes exist in the haloes, but their mass is usually far smaller than that of the central black hole in these haloes, where one galaxy dominates the stellar mass. The results remain unchanged if we reduce the search radius for the most massive BH. We also track $M_{\rm BH}$ for our secular sample at high time cadence in Section 5, where we correlate changes in $M_{\rm BH}$ with CGM properties. While we do not filter this sample for major BH mergers, we expect the BH growth for the secular sample to be dominated by gas accretion, given that we filter out galaxy (and their associated BH) major mergers by definition of this sample.

2.3.2 *Absorber column densities*

Ion column densities are calculated by projecting SPH particles on to a two-dimensional map as described by for example Oppenheimer et al. (2018). Ionization fractions for a range of species, including H I, C IV, and O VI are calculated using CLOUDY-calculated lookup tables as a function of density, temperature, and redshift. Calculations assume ionization equilibrium, and include collisional ionization and photoionization from the time-evolving Haardt & Madau (2001) background that was also used for the calibration of the cooling rates during the simulation. We use the self-shielding prescription of Rahmati et al. (2013) for H I column densities, although this does not affect our covering fraction calculations. We include gas only within a radius of $3 \times R_{200}$ from the centre of the galaxy, which separates out contamination from the CGM of neighbouring galaxies (e.g. Oppenheimer et al. 2018). Three perpendicular projections are used to calculate covering fractions.

2.3.3 Galaxy colours

We use the `SKIRT` radiative transfer dust-attenuated colours, which are available in the data release of Camps et al. (2018). We use the Sloan Digital Sky Survey (SDSS) u and r-band absolute magnitudes to calculate $u - r$ colours for a random orientation of each galaxy. We report $u - r$ colours back to $z = 2.5$, using their rest-frame colours.

3 THE DEPENDENCE OF THE CGM ON THE CENTRAL BLACK HOLE

We begin this section by casting the large-scale physical parameters of galactic haloes in terms of integrated feedback energies compared to gaseous halo binding energies, and then focus on the variety of CGM and galactic properties of MW-mass haloes. We also discuss energy budgets of stellar and BH feedback in terms of CGM gas fractions.

Fig. 1 plots $f_{\rm CGM}$ as a function of M_{200}. This was the central plot in D19 (their figs 1 and 2), where they coloured the data points by the scatter in other parameters, finding a strong anticorrelation between $f_{\rm CGM}$ and $M_{\rm BH}$ at fixed M_{200}. In the left-hand panel, we colour our data points by the ratio of the integrated feedback energy from the central BH, $E_{\rm BH}$ from equation (2), to the binding energy of the baryons in the halo, $\widetilde{E}^b_{\rm bind}$, where

$$\widetilde{E}^b_{\rm bind} = \frac{1}{2} f_{\rm b} \frac{G M_{200}^2}{R_{200}} \qquad (3)$$

and G is the gravitational constant and $f_{\rm b} \equiv \frac{\Omega_{\rm b}}{\Omega_{\rm M}}$. $\widetilde{E}^b_{\rm bind}$ also equals $\frac{1}{2} f_{\rm b} M_{200} v_{200}^2$, where $v_{200} = \sqrt{G M_{200}/R_{200}}$. We emphasize that this is an analytic approximation of the $E^b_{\rm bind}$ calculated by Davies et al. (2019b) from matched haloes in the EAGLE dark matter-only (DMO) simulation as described in their Section 5.[1] We use opaque (faded) circles to indicate whether $M_{\rm BH}/M_{200}$ is greater (less) than 10^{-5}. The black line shows the running median $f_{\rm CGM}(M_{200})$ value for the opaque points, while the grey line indicates the median for faded points having higher gas fractions. The nearly vertical colour gradient of opaque points indicates $f_{\rm CGM}$ depends on $E_{\rm BH}/\widetilde{E}^b_{\rm bind}$ at $M_{200} = 10^{12}$–$10^{13}\,{\rm M}_{\odot}$ when $M_{\rm BH}/M_{200} > 10^{-5}$. We bracket the $10^{12.0}$–$10^{12.3}\,{\rm M}_{\odot}$ haloes, because this slice shows the greatest diversity in $f_{\rm CGM}$ from having their gaseous haloes being nearly completely evacuated to retaining ~ 50 per cent of their cosmic baryon fraction. We will later argue $f_{\rm CGM}$ is related to the diverse set of galactic properties of their centrals.

We reverse the shading in the right-hand panel to highlight the $M_{\rm BH}/M_{200} < 10^{-5}$ haloes. These haloes do not show a clear dependence of $f_{\rm CGM}(M_{200})$ on $E_{\rm BH}$, suggesting that BH feedback becomes efficient at ejecting CGM only above $M_{\rm BH}/M_{200} \gtrsim 10^{-5}$ for MW-mass haloes, i.e. $M_{\rm BH} \gtrsim 10^{7.0-7.3}\,{\rm M}_{\odot}$, as shown by Bower et al. (2017).

We now focus on our M^* sample, showing data points of $f_{\rm CGM}$ against $M_{\rm BH}$ in the left-hand panel of Fig. 2, where the three solid lines indicate running medians for 0.1-dex M_{200} bins. We expand this analysis to the L^* sample showing dashed lines for $M_{200} < 10^{12.0}$ and $>10^{12.3}\,{\rm M}_{\odot}$. The link between $M_{\rm BH}$ and $f_{\rm CGM}$ is muddled without knowledge of M_{200}, because a small change in halo mass results in a different $f_{\rm CGM}(M_{\rm BH})$.

The right-hand panel of Fig. 2 considers the halo potential, by plotting $f_{\rm CGM}$ as a function $E_{\rm BH}/\widetilde{E}^b_{\rm bind}$ in the left subpanel. The running medians for the same five halo mass bins show much more overlap than in the left-hand panel, which indicates that CGM ejection depends on the ability of the integrated black hole energy to overcome the binding energy of the halo. $E_{\rm BH}/\widetilde{E}^b_{\rm bind}$ is a more essential scaling because it controls for the halo mass dependence of gravitational potential depth. The colour scale of the data points indicates $M_{\rm BH}$ closely tracks this quantity with the only difference being the $\widetilde{E}^b_{\rm bind}$ in the denominator.[2] Four $E_{\rm BH}/\widetilde{E}^b_{\rm bind}$ quartiles are indicated by black dots with x-axis error bars indicating ranges and y-axis error bars indicating $1-\sigma$ dispersions of $f_{\rm CGM}$ for each quartile. These quartiles define our samples starting in Section 5, where we discuss how the CGM responds to BH growth episodes.

The running medians diverge at small $E_{\rm BH}/\widetilde{E}^b_{\rm bind}$, which indicates that more massive haloes with low-mass black holes retain more baryons. This suggests that stellar feedback likely plays a larger role in clearing lower mass haloes than AGN feedback. We consider the ratio of $E_*/\widetilde{E}^b_{\rm bind}$ (right subpanel), where E_* is the sum of integrated SF-driven feedback, which has been stored in EAGLE outputs. The values for E_* usually exceed $E_{\rm BH}$, but the $E_*/\widetilde{E}^b_{\rm bind}$ values are limited to a smaller range by the definition of the M^* sample's stellar mass range. There is a weaker trend of $f_{\rm CGM}$ declining with $E_*/\widetilde{E}^b_{\rm bind}$, but we argue this arises from more evacuated haloes having preferentially earlier star formation, which leads to higher efficiency stellar feedback in the EAGLE prescription (as explained in Crain et al. 2015) and an overall greater E_* for a given stellar mass.

Stellar feedback, which heats gas particles to $10^{7.5}$ K in EAGLE, is less efficient at clearing out the CGM than BH feedback. Stellar feedback leads to gas buoyantly rising into the CGM (e.g. Bower et al. 2017; Oppenheimer 2018), but this gas often cools and recycles back on to the galaxy. This indicates a fundamental distinction with BH feedback, which delivers more energy per heating event. E_* is delivered more steadily than $E_{\rm BH}$, and a greater fraction of this energy is lost to radiative cooling. Stellar feedback materials can be cycled through a sequence of superwind outflows, re-accretion on to the galaxy, and further star formation and outflows in a sequence often termed the 'baryon cycle'. The $E_{\rm BH}$ feedback, which heats gas to $10^{8.5}$ K, does not suffer as much radiative losses. Therefore, BH feedback can disrupt or at least significantly alter this baryon cycle by curtailing the supply of re-accreting gas available in the CGM.

---

[1] The typical values Davies et al. (2019b) are higher than $\widetilde{E}^b_{\rm bind}$ by a factor of $\sim$5 owing to a combination of centrally concentrated DM profiles and additional mass outside R_{200}. We also note that $\widetilde{E}^b_{\rm bind}$ is smaller by 1/6th than unbinding a uniform density sphere of mass $f_{\rm b} M_{200}$, which is $3/5 f_{\rm b} G M_{200}^2/R_{200}$.

[2] Using the quantity $M_{\rm BH}/\widetilde{E}^b_{\rm bind}$ gives equivalent results given EAGLE's BH feedback assumes $E_{\rm BH} \propto M_{\rm BH}$, but we use the unitless energy ratio parametrization.

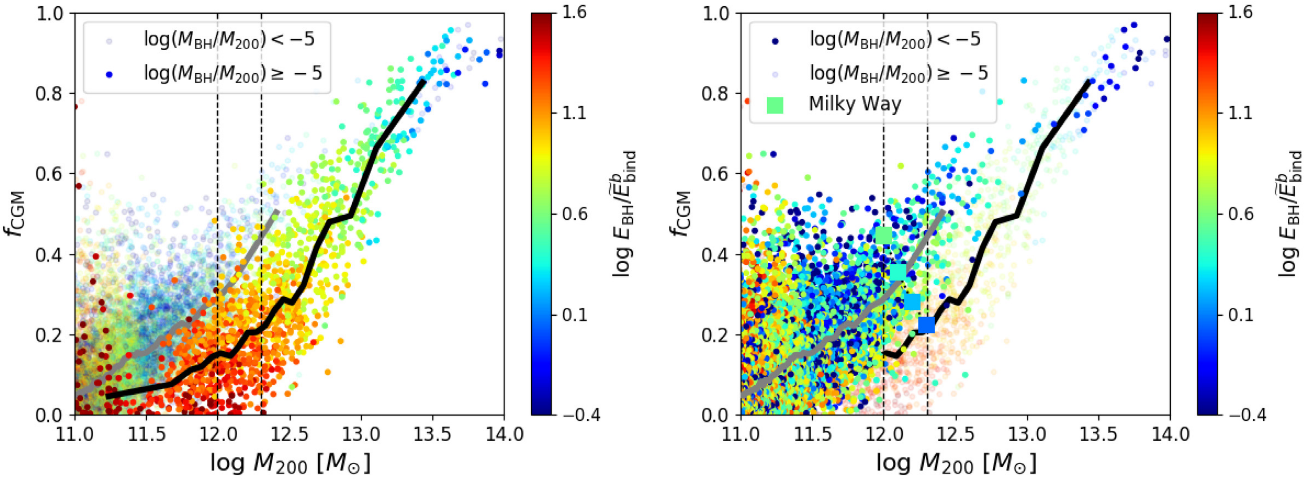

Figure 1. Halo gas fraction as a function of halo mass in EAGLE, coloured by the integrated energy of BH feedback divided by the gaseous halo binding energy. Galaxies with black hole masses $\geq$ (<) $10^{-5}M_{200}$ are plotted in solid in the left-hand (right-hand) panel, and their median is shown as a black (grey) line. $E_{\rm BH}/\widetilde{E}^b_{\rm bind}$ shows a nearly vertical gradient with $f_{\rm CGM}(M_{200})$ in the galaxy halo regime in the left-hand panel, indicating the integrated feedback from black holes is anticorrelated with $f_{\rm CGM}$ when $M_{\rm BH}/M_{200} \geq 10^{-5}$. The best estimate for the Milky Way-like halo masses is shown using large squares for four estimates of halo masses spanning our M^* regime from $10^{12.0-12.3}$ $\rm M_\odot$ (e.g. McMillan 2011; Eadie & Jurić 2019) bounded by grey dashed lines.

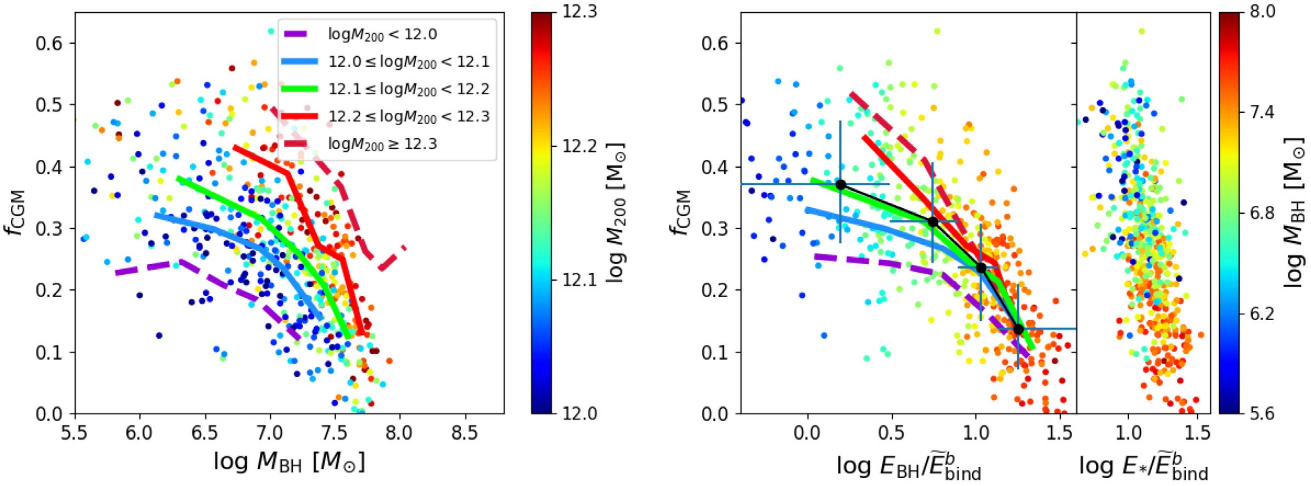

Figure 2. *Left-hand panel:* Halo gas fraction as a function of black hole mass for central galaxies with $M_* = 10^{10.2-10.7}$ $\rm M_\odot$ and $M_{200} = 10^{12.0-12.3}$ $\rm M_\odot$, coloured by halo mass. We also show median relations in solid lines for three 0.1 dex halo bins, and include two dashed lines for all haloes hosting $M_* = 10^{10.2-10.7}$ $\rm M_\odot$ galaxies below $10^{12.0}$ and above $10^{12.3}$ $\rm M_\odot$, for which points are not included. *Right-hand panel:* The same haloes are plotted as a function of the ratio of the integrated $E_{\rm BH}$ over $\widetilde{E}^b_{\rm bind}$, coloured by $M_{\rm BH}$ in the left subpanel. The median curves for the different halo mass bins now converge at high-$E_{\rm BH}/\widetilde{E}^b_{\rm bind}$ values, indicating this relation is more important for $f_{\rm CGM}$. Four quartiles of $E_{\rm BH}/\widetilde{E}^b_{\rm bind}$ are shown as black points with error bars indicating $1-\sigma$ dispersions for $f_{\rm CGM}$ and the ranges of each quartile. The right subpanel shows the integrated stellar feedback energy, which is almost always greater than $E_{\rm BH}$, but does not show a correlation with $f_{\rm CGM}$.

4 OBSERVATIONAL INDICATORS OF THE CGM BARYON FRACTION

We have argued for a link between two physical quantities: the energy released by the BH relative to the halo binding energy and the fraction of a halo's baryons in the CGM. While direct measurements of these quantities are impossible to obtain, we focus here on the latter quantity – observational strategies to access the CGM baryon fraction accessible with current instrumentation. Before continuing, we note that we do not attempt to find observational proxies for $E_{\rm BH}$ beyond assuming a linear proportionality to $M_{\rm BH}$. Because the very few existing measurements of $M_{\rm BH}$ for L^* galaxies are all in the local Universe (Kormendy & Ho 2013), we require that our $f_{\rm CGM}$ proxy is also locally available.

We calculate median CGM observational measurements across four quartiles of $M_{\rm BH}$ in the M^* sample to determine how each relates to $f_{\rm CGM}$. The median value of the lowest (highest) quartile of $M_{\rm BH}$ is $10^{6.42}$ ($10^{7.58}$) $\rm M_\odot$, where $f_{\rm CGM} = 0.35$ (0.14). We consider several ions commonly observed with COS, including H I, C IV, and O VI. Our favoured $f_{\rm CGM}$ proxy is the C IV covering fraction of absorbers with column densities $N_{\rm C\,IV} > 10^{13.5}$ cm^{-2} within a circle of radius

100 kpc ($C_{\rm C\,IV>13.5,100\,kpc}$) plotted as a function of $M_{\rm BH}$ in Fig. 3, left-hand panel. We find that this quantity declines by nearly a factor of two from a median with scatter of $C_{\rm C\,IV>13.5,100\,kpc} = 0.79^{+0.10}_{-0.15}$ to $0.43^{+0.24}_{-0.27}$ from the lowest to highest $M_{\rm BH}$ quartile in EAGLE. There are three main lines of reasoning we use in evaluating the different ions.

The first reason we favour C IV is because the 1548, 1551 Å doublet is available via COS in the very local Universe ($z \lesssim 0.01$) and has been observed in many existing COS surveys, (e.g. Bordoloi et al. 2014; Liang & Chen 2014; Borthakur et al. 2015; Burchett et al. 2015; Berg et al. 2018). These previous samples of galaxy–QSO pairs that cover C IV within the inner CGM (R < 100 kpc) of 0.1–1L^* galaxy haloes amount to approximately 90 sightlines in total. Future archival surveys of COS data combined with deep galaxy spectroscopic redshifts, including the *CGM*^{2} Survey (led by J. Werk), will expand the total number of sightlines within 100 kpc covering C IV at $z < 0.1$ by at least a factor of two. We select $N_{\rm C\,IV} = 10^{13.5}$ cm^{-2} as the column density threshold because this value is easily detectable in existing UV spectra probing the CGM. For reference, it corresponds to an equivalent width of ≈100 mÅ for the strong line of the doublet at 1548 Å, which is detectable at 3σ in an S/N ≈5–8 COS sightline using the G160M grating.

The second reason we choose $C_{\rm C\,IV>13.5,100\,kpc}$ is that its decline mirrors $f_{\rm CGM}$ for physically meaningful reasons. C IV is a tracer of metals for temperatures 10^4–10^5 K and densities 10^{-5}–10^{-3} cm^{-3} at $z = 0$ (e.g. Schaye et al. 2003; Oppenheimer & Davé 2006; Davé & Oppenheimer 2007; Ford et al. 2013; Rahmati et al. 2016). C IV is photoionized by the UV background at $T < 10^5$ K for lower densities and collisionally ionized at $\sim 10^5$ K for higher densities, but these two regimes are relatively close to each other in density–temperature phase space, which we argue make C IV a good tracer of a well-defined region of the phase space of the diffuse CGM. This ion still misses the majority of the CGM baryons, which typically have $T \sim 10^4$–10^7 K and $n_{\rm H} \sim 10^{-5}$–10^{-2} cm^{-3} in MW-mass haloes.

A third reason for $C_{\rm C\,IV>13.5,100\,kpc}$ is that its decline in covering fraction roughly follows its decline in mean CGM column density within 100 kpc (Fig 3, right-hand panel). The log $\langle N_{\rm C\,IV,100\,kpc}\rangle$/cm^{-2} declines from 14.05 to 13.72 from the lowest to highest quartiles. The similar decline in $C_{\rm C\,IV}$ and $\langle N_{\rm C\,IV}\rangle$ (i.e. a factor of ≈2) indicates that C IV is an effective tracer of the diffuse CGM.

The global C IV column density distributions reported in EAGLE (Rahmati et al. 2016) show reasonable agreement with observational surveys (Cooksey et al. 2010; Burchett et al. 2015; Danforth et al. 2016). For the CGM, EAGLE shows very good agreement for C IV observed around $z \approx 2$ star-forming galaxies (Turner et al. 2017), but a comparison between $N_{\rm C\,IV}$ and low-z EAGLE galaxies has yet to be published. Chen, Lanzetta & Webb (2001) and Liang & Chen (2014) observe strong C IV inside 100 kpc for galaxies in the L^* mass range, followed by a rather steep decline beyond ≈100 kpc. Bordoloi et al. (2014) and Burchett et al. (2016) studied C IV in the haloes of galaxies over a wider mass range, finding similarly declining profiles. We note here that the average C IV profiles around low-z galaxies reported in Oppenheimer et al. (2018) appear consistent with observations, and that the $N_{\rm C\,IV}$ measurements by Burchett et al. (2016) for $M_* > 10^{10}$ M$_\odot$ inside 100 kpc (their figs 3 and 5) are in the range of $\langle N_{\rm C\,IV,100\,kpc}\rangle$ values in Fig. 3.

We list CGM measures for the lowest and highest $M_{\rm BH}$ quartiles in Table 1, where we also consider O VI and H I values repeating our three lines of reasoning used for C IV. The O VI 1032, 1038 Å doublet is not locally available via COS; however, the readily detectable covering fraction, $C_{\rm O\,VI>13.7,100\,kpc}$, shows a significant decline, which is matched by a decline in $\langle N_{\rm O\,VI,100\,kpc}\rangle$ indicating it is an effective tracer of the diffuse CGM. We discuss the prospects and interpretation of O VI further in Section 7.1.

H I is detected ubiquitously in the CGM of local galaxies via the 1216 Å Lyα transition (e.g. Tumlinson et al. 2013; Borthakur et al. 2015; Keeney et al. 2017). While we find $C_{\rm H\,I>15.0,100\,kpc}$ is a good metric for separating the lowest and highest $M_{\rm BH}$ quartiles in Table 1, $N_{\rm H\,I} = 10^{15.0}$ cm^{-2} becomes saturated in Lyα. Furthermore, $\langle N_{\rm H\,I,100\,kpc}\rangle$ is 3-4 orders of magnitude higher than this limit, which implies a highly clumpy CGM tracer where most H I arises from gas with a small filling factor (Ford et al. 2014, Horton et al. in prep).

Finally, we discuss the use of covering fractions calculated from an $r = 100$ kpc cylinder to determine the baryon content of a sphere ($f_{\rm CGM}$). We calculate mean hydrogen and oxygen column densities using the cylinder and report median CGM $\langle N_{\rm H,100\,kpc}\rangle$ and $\langle N_{\rm O,100\,kpc}\rangle$, where we excise the ISM (any gas particles with non-zero SFR) for the quartiles in Table 1. $\langle N_{\rm H,\,CGM}\rangle$ declines by −0.29 dex, while $\langle N_{\rm O,\,CGM}\rangle$ declines by −0.40 dex with increasing $M_{\rm BH}$, which nicely reflects the decline in $f_{\rm CGM}$ as well as C IV and O VI covering fraction indicators. We can also calculate the CGM metallicity, which declines by −0.11 dex from $12 + \log({\rm O/H})_{\rm CGM} = 8.43$ to 8.32. Although the CGM metallicity declines as $M_{\rm BH}$ increases, it is a 3.5 times smaller decrease than the decline of baryons within the CGM and 2.6 times smaller than the baryons in a cylinder extending to $3 \times R_{200}$ on either side of the galaxy. We also check CGM metallicity excluding $n_{\rm H} > 10^{-3.0}$ cm^{-3} gas, and find the same decline in metallicity, with Z shifted by −0.1 dex. The geometrical effect of tracing baryons in a 100 kpc radius cylinder versus a sphere of radius R_{200} manifests itself in the respective values of $\langle N_{\rm H,\,CGM}\rangle$ versus $f_{\rm CGM}$, where the former declines by approximately one-third less, because baryons pushed out beyond R_{200} remain in the cylinder along one dimension.

5 THE EVOLUTION OF THE CGM AND CENTRAL BLACK HOLES

One of our central goals of this work is to catch the process of baryon ejection from the CGM in the act and determine if it is a direct result of BH feedback. To do this, we use the rich data set of EAGLE snipshot outputs that follow galaxies, BHs, and the CGM in up to 155 outputs between $z = 5$ and 0 for our *secular* sample comprised of 246 galaxies. Fig. 4 shows examples of the evolution of a blue, star-forming galaxy (left) and a red, passive (right) galaxy residing in similar mass haloes ($M_{200} \approx 10^{12.15}$ M$_\odot$), resulting in similar mass galaxies ($M_* \approx 10^{10.6}$ M$_\odot$). The plotting begins when M_* exceeds $10^{9.5}$ M$_\odot$. We also list the final $z = 0$ $u - r$ colours in the upper panels.

The upper panels show the halo mass (black), the stellar mass inside an aperture of 30 kpc (red), and the central BH mass (cyan), where the latter are selected to be very different ($M_{\rm BH} = 10^{6.3}$ versus $10^{7.7}$ M$_\odot$). We have chosen examples in the lowest and highest quartiles of $E_{\rm BH}/\tilde{E}^b_{\rm bind}$ to focus on how rapid BH growth and the associated feedback transform the CGM, which for the right galaxy begins soon after $z = 1$. The middle panels show $f_{\rm CGM}$, which is relatively flat and slightly declining for the blue galaxy, but sharply dips for the eventual red galaxy first at $z = 0.7$ as the BH grows by 2×10^7 M$_\odot$, and then again at $z = 0.4$ as another episode of rapid BH growth increases the mass by 1.3×10^7 M$_\odot$.

The lower panels show the time-evolving C IV covering fractions in blue mirroring the decline in $f_{\rm CGM}$. The evolution of $C_{\rm C\,IV}$ is due to

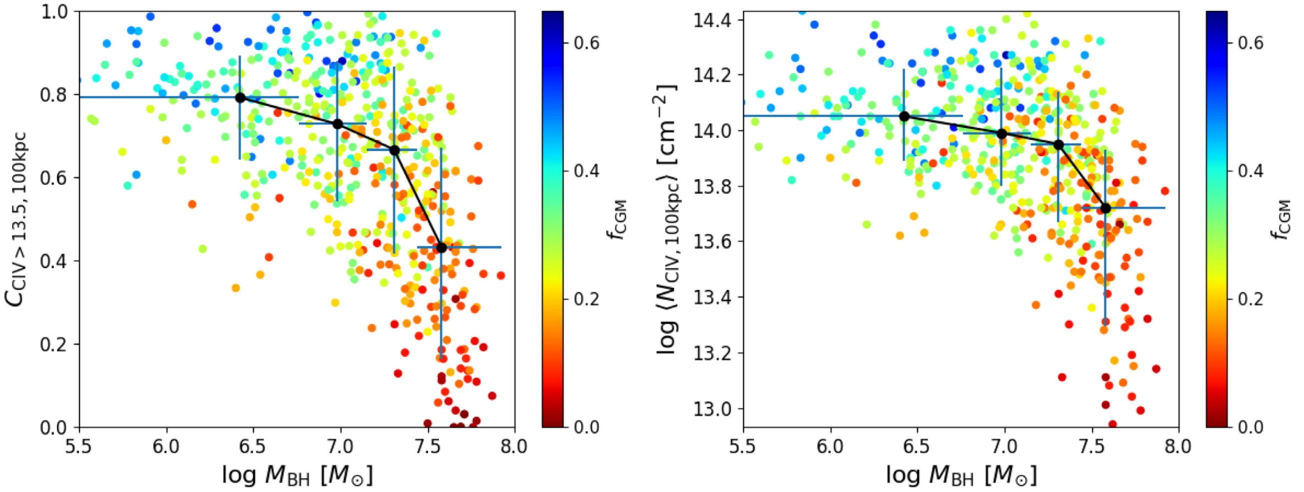

Figure 3. *Left-hand panel:* Covering fraction of C IV absorbers with column densities greater than $10^{13.5}$ cm^{-2} inside a circle of radius 100 kpc as function of $M_{\rm BH}$ for the M^* sample at $z = 0$. $C_{\rm C\,IV>13.5,100\,kpc}$, which is observable around local galaxies, is a good observational proxy for $f_{\rm CGM}$ (the colour of the data points), which declines the most for the highest mass black holes ($M_{\rm BH} > 10^{7.4}$ M$_\odot$). *Right-hand panel:* The mean C IV column density, $\langle N_{\rm C\,IV,100\,kpc}\rangle$, inside the same radius 100 kpc circle also shows a decline with $M_{\rm BH}$. The covering fraction is a simpler statistic to obtain, because $N_{\rm C\,IV}$ measurements can be difficult or uncertain if the absorption is saturated.

Table 1. EAGLE CGM values for the lowest and highest BH mass quartiles in the M^* sample at $z = 0$.

Metric[1]	Low $M_{\rm BH}$	High $M_{\rm BH}$	Difference
log $M_{\rm BH}$/M$_\odot$	6.42	7.58	1.16 dex
$f_{\rm CGM}$	0.35	0.14	– 0.39 dex
$C_{\rm C\,IV>13.5,100\,kpc}$	$0.79^{+0.10}_{-0.15}$	$0.43^{+0.24}_{-0.27}$	– 0.26 dex
log $\langle N_{\rm C\,IV,100\,kpc}\rangle$/cm^{-2}	14.05	13.72	– 0.33 dex
$C_{\rm O\,VI>13.7,100\,kpc}$	$0.81^{+0.12}_{-0.17}$	$0.32^{+0.28}_{-0.23}$	– 0.40 dex
log $\langle N_{\rm O\,VI,100\,kpc}\rangle$/cm^{-2}	14.03	13.67	– 0.36 dex
$C_{\rm H\,I>15.0,100\,kpc}$	$0.64^{+0.12}_{-0.19}$	$0.33^{+0.24}_{-0.21}$	– 0.29 dex
log $\langle N_{\rm H\,I,100\,kpc}\rangle$/cm^{-2}	18.76	17.92	– 0.84 dex
log $\langle N_{\rm H,100\,kpc}\rangle$/cm^{-2}	19.84	19.55	– 0.29 dex
log $\langle N_{\rm O,100\,kpc}\rangle$/cm^{-2}	16.27	15.87	– 0.40 dex
12 + log (O/H)$_{\rm 100\,kpc}$	8.43	8.32	– 0.11 dex

[1] Median values of all haloes in each quartile reported. 1σ scatter reported for halo covering factions.

several effects including (1) the metal enrichment of the CGM, (2) the changing ionization field assuming a Haardt & Madau (2001) background, and (3) the growth of the R_{200}, which is smaller than 100 physical kpc at high-z and more than twice as large at $z = 0$. We also show O VI and H I covering fractions within 100 kpc for these haloes in the lower panel, which also both respond to the rapid BH growth episodes for the passive galaxy.

Instead of focusing on two examples, we plot all galaxies in the secular sample in the lowest and highest quartiles of $E_{\rm BH}/\widetilde{E}^{b}_{\rm bind}$ in Fig. 5. Individual galaxies are shown with thin lines, but we show the median for each sample along with 16–84 per cent shaded spreads. All galaxies (61 in each sample) are tracked back to $z = 1.487$ (vertical dotted line), though the sample thins out at earlier times as lower mass galaxies fall out of the sample, if $M_* < 10^{9.5}$ M$_\odot$. Additionally, major mergers can occur in our sample at this epoch, which also contributes to the sawtooth behaviour as new lower mass galaxies join the sample at snapshot outputs corresponding to z =1.737, 2.012, 2.237, 2.478, 3.017, 3.528, and so on. Even though we identify galaxies between $z = 1.487$ and 0 without major mergers using 13 snapshots, mergers can slip into our sample when examining high-cadence snipshots, though at a level that does not alter the conclusions we draw.

The stellar populations of the highest $E_{\rm BH}/\widetilde{E}^{b}_{\rm bind}$ haloes assemble earlier than their lowest $E_{\rm BH}/\widetilde{E}^{b}_{\rm bind}$ counterparts, resulting in a population of galaxies with much less late-time growth and redder $z = 0$ colours ($u - r = 2.23$ versus 1.68). It is crucial to avoid the impression that these two sets of haloes are the same but for their BH masses, because D19 demonstrated that the haloes with higher mass BHs have (1) earlier formation times, (2) higher concentrations, and (3) greater intrinsic binding energies (calculated particle-by-particle using a matched DM-only simulation that is devoid of baryonic effects). Over the last 9.5 Gyr of evolution, the high-$E_{\rm BH}/\widetilde{E}^{b}_{\rm bind}$ haloes increase their stellar masses from $10^{10.2}$ to $10^{10.4}$ M$_\odot$, while the low-$E_{\rm BH}/\widetilde{E}^{b}_{\rm bind}$ haloes increase from $10^{9.8}$ to $10^{10.5}$ M$_\odot$, a factor of 3 times more. Hence, while we are focusing on secular evolution, our two sets of haloes have fundamentally different evolutionary histories, which D19 emphasize by showing the counter-intuitive relationship that more tightly bound haloes end up with more evacuated CGMs through greater integrated BH feedback.

The second panel in Fig. 5 following central BH masses shows two very different tracks by design of our two samples. The BH masses are near the seed mass at $z = 2{-}3$ for both samples, but the high-$E_{\rm BH}/\widetilde{E}^{b}_{\rm bind}$ haloes have the highest rate of growth at $z > 1$. The medians jump around at $z > 1.487$ as new galaxies are added to the sample, but some of the individual $M_{\rm BH}$ time histories of the low-$E_{\rm BH}/\widetilde{E}^{b}_{\rm bind}$ haloes in cyan move up then down as more massive BHs can temporarily pass within 50 kpc of the galaxy. No BH masses overlap between the two samples at $z = 0$ (by sample construction) and the median BH masses are $10^{6.4}$ versus $10^{7.6}$ M$_\odot$.

Next we consider the evolution of the CGM, starting with $f_{\rm CGM}$, which begins just above $f_{\rm CGM} = 0.5$ and declines with time for both samples to their $z = 0$ values (0.33 versus 0.12), which agree closely with the values reported for the two quartiles of the M^* sample (Fig. 2, right-hand panel). The CGM fractions appear to respond to

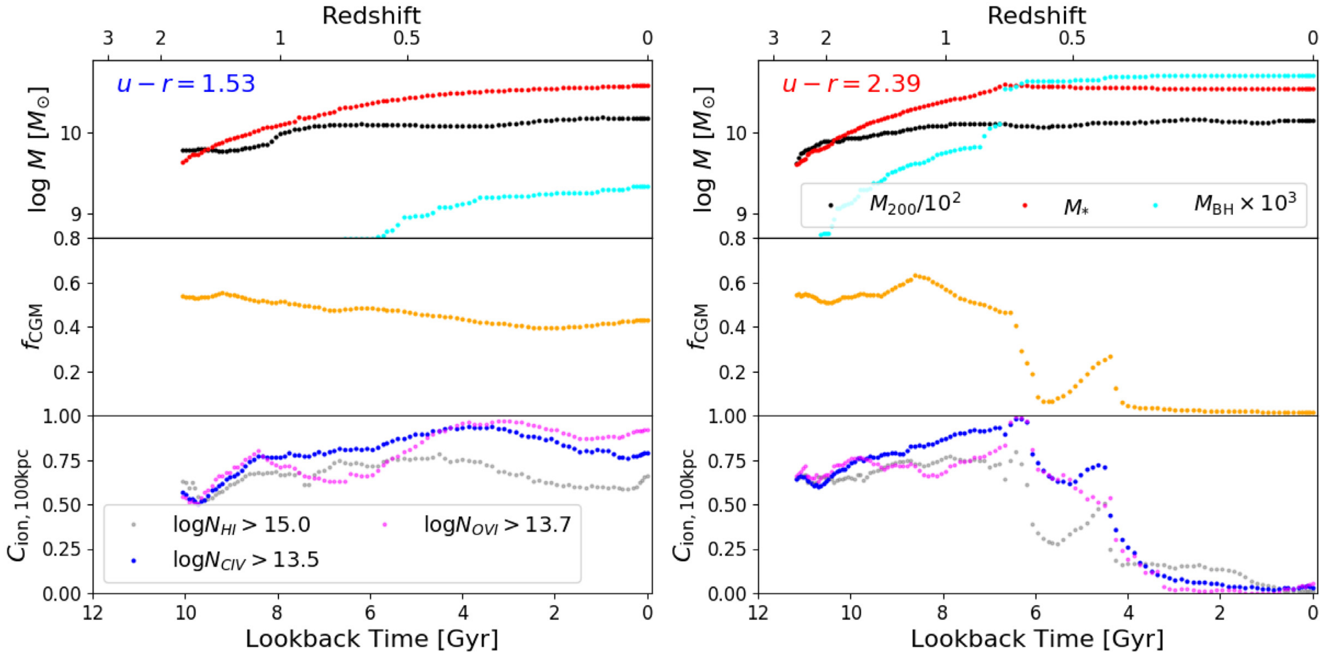

Figure 4. The example time histories of two secularly evolving galaxies with a low $M_{\rm BH}$ (left-hand panels) and a high $M_{\rm BH}$ (right-hand panels). Upper panels show the mass evolution of M_{200} (black), M_* (red), and the central black hole (cyan). The middle panel shows the CGM baryon content, $f_{\rm CGM}$, in orange. Covering fractions of several ions, including C IV ($C_{\rm C\,IV>13.5,100\,kpc}$ in blue) are plotted to show how these CGM observational proxies respond to the evolving baryon content. The growth of the black hole on the right causes a reduction of $f_{\rm CGM}$ soon after that is reflected in C IV and other ions. The galaxy on the left remains in the blue cloud at $z = 0$, while the galaxy on the right joins the passive sequence soon after its rapid BH growth at $z = 0.7$. Present-day $u - r$ values are listed in the upper left of the upper panels.

the growth of $M_{\rm BH}$ with the greatest change in the high-$E_{\rm BH}/\widetilde{E}^b_{\rm bind}$ haloes occurring at epochs around $z = 1$.

The C IV covering fraction (Fig. 5, lower panel) also shows a response to BH growth, but it appears delayed relative to $f_{\rm CGM}$ for the high-$E_{\rm BH}/\widetilde{E}^b_{\rm bind}$ haloes as $C_{\rm C\,IV}$ declines between $z = 1$ and 0.3. To better track how baryon clearing is linked to the BH, we shift a set of the high-$E_{\rm BH}/\widetilde{E}^b_{\rm bind}$ time histories to the snipshot interval with the largest total BH growth, $t_{\Delta M_{\rm BH,max}}$. Fig. 6 plots these shifted time histories for galaxies with BH growth episodes at least 2×10^6 M$_\odot$ between snipshots separated by <100 Myr and at $z > 0.47$ to allow at least 5 Gyr of subsequent evolution. The sample contains 31 galaxies, although the trends we now discuss are only slightly weaker if we include the other 30 galaxies.

Very little stellar assembly occurs after $t_{\Delta M_{\rm BH,max}}$ (upper panel) as the galaxy's M_* essentially flatlines in response to the biggest BH growth episode in the galaxy's history (second panel). The average $M_{\rm BH}$ increases by roughly 5-fold in the preceding 500 Myr, though our sample is not uniform further back as $t_{\Delta M_{\rm BH,max}}$ can occur at high redshifts with little further history. We see a clear decline in $f_{\rm CGM}$ (third panel) at $t_{\Delta M_{\rm BH,max}}$ indicating that there is indeed a causal link with BH growth. This significant growth episode of the BH leads to a reduction of $f_{\rm CGM}$ by a factor of nearly two within 1 Gyr. This is the most clear indication that an active, rapid BH growth episode can clear much of the CGM.

However, as expected from Fig. 5, $C_{\rm C\,IV>13.5,100\,kpc}$ does not respond as dramatically to the BH growth, and in fact first jumps up from 0.76 to 0.87 in the 500 Myr after the BH growth episode. Despite the initial bump, the covering fraction has fallen to 0.49 by 4 Gyr. While we argue C IV is a good proxy for $f_{\rm CGM}$ at $z = 0$ in Section 4, we predict this ion's covering fraction evolution is not a good tracer for $f_{\rm CGM}$ during the actual process of baryon ejection from the halo. $C_{\rm C\,IV}$ increases in response to BH feedback before declining, while $f_{\rm CGM}$ declines straight away. Therefore, an observing program targeting the progenitors of passive galaxies undergoing CGM clearing at higher redshift may have to take a different approach than using just $C_{\rm C\,IV}$, and may rely on identifying kinematic indicators of outflows extending into the CGM.

To disentangle the connection between BH growth, $f_{\rm CGM}$, and our covering fraction tracers, we apply a time series analysis, where we correlate all tracked BH growth on intersnipshot intervals (33−125 Myr) with any change in CGM properties. For each $E_{\rm BH}/\widetilde{E}^b_{\rm bind}$ halo time history in the high-$E_{\rm BH}/\widetilde{E}^b_{\rm bind}$ secular sample, we calculate a series of Pearson correlation coefficients, ρ, between $\Delta M_{\rm BH}$ and the change in either $f_{\rm CGM}$ or a covering fraction using all available snipshots. If we take the time series of $\Delta M_{\rm BH}$ and calculate its ρ with the $\Delta f_{\rm CGM}$ time series, we expect a negative value if the BH nearly immediately ejects baryons from the CGM. This is seen in Fig. 7 when we consider the correlation with $\Delta f_{\rm CGM}$ at $t = t_{\Delta M_{\rm BH}}$ (thick orange line intersecting with vertical dotted grey line), which shows the mean ρ for all high-$E_{\rm BH}/\widetilde{E}^b_{\rm bind}$ haloes. This data point alone does not necessarily indicate that the current BH growth episode is responsible for the decline in $f_{\rm CGM}$, because BH growth episodes are clustered in time (Fig. 6) and previous BH feedback could drive baryons out of the CGM.

We wish to identify the evolution in the correlation between CGM quantities and BH growth, therefore we apply time lag shifts of a CGM quantity time series relative to the BH growth time series, and plot a series of correlation coefficients as a function of time lag in Fig. 7. For example, the curves crossing at $t - t_{\Delta M_{\rm BH}} = 1$ Gyr indicate the correlation of the change in CGM quantities with the BH growth activity 1 Gyr earlier. We plot the mean ρ values of all haloes at each time lag creating a continuous line, demonstrating the

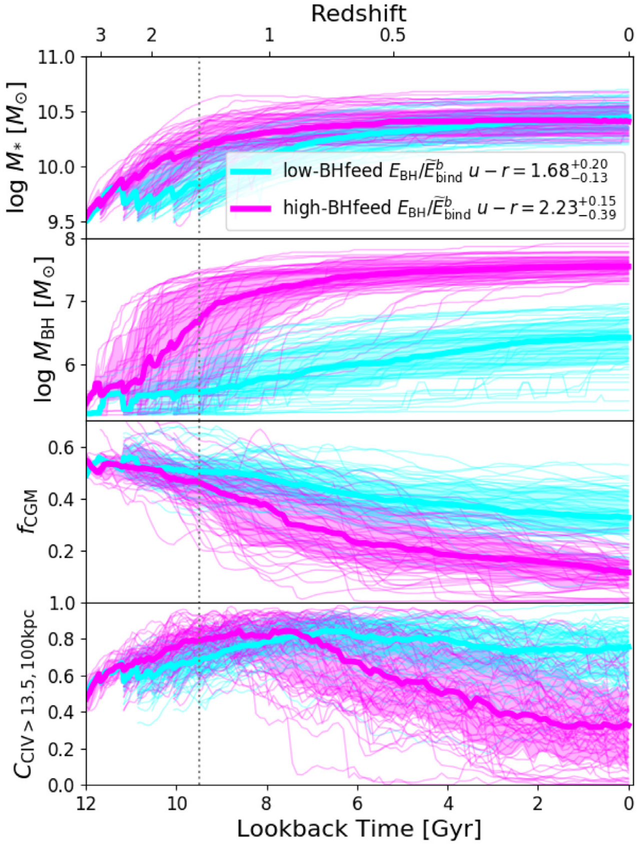

Figure 5. The time evolution of two samples of secularly evolving galaxies, those in the lowest (highest) quartile of the cumulative BH feedback energy divided by gaseous halo binding energy, $E_{\rm BH}/\widetilde{E}^b_{\rm bind}$, are plotted in cyan (magenta) as a function of lookback time. Median histories are shown in solid lines with shading indicating $1-\sigma$ spreads. The panels from top to bottom show stellar masses, black hole masses (which differ by sample construction), CGM gas fractions, and C IV covering fractions within 100 kpc. Gas fractions are similar for the two samples at $z \gtrsim 2$, but decline more for the high-BH feedback sample, which leads to less star formation and stellar growth. C IV traces the decline in $f_{\rm CGM}$ since $z=1$, although at higher redshift it shows a faster rise as enrichment of the CGM proceeds faster with more star formation occurring at these early epochs. The grey dotted vertical line indicates the redshift after which all galaxies in each sample are tracked.

typical time-evolving relationship between a CGM variable and the BH growth. The time lag evolution of the correlation between $\Delta f_{\rm CGM}$ and $\Delta M_{\rm BH}$ value reaches its nadir 300 Myr after $t_{\Delta M_{\rm BH}}$, indicating that CGM ejection peaks at this time-scale after BH growth. In fact, the correlation coefficient becomes sharply more negative right after $t_{\Delta M_{\rm BH}}$ indicating an immediate acceleration of baryon ejection, likely through shocks propagating through the CGM at supersonic speeds. The overall sharp dip in the orange line is the clearest indication that EAGLE BHs are responsible for ejecting their CGMs in short order ($\lesssim$ 100 Myr). The negative ρ values before $t_{\Delta M_{\rm BH}}$ are likely due to BH growth episodes (AGN activity) being clustered in time, but could also arise from enhanced SF activity and feedback preceding the AGN ejecting baryons from the halo. The absolute values of ρ are less important than the relative values, but given that most $\Delta M_{\rm BH}$ values are very small, the mean Pearson $\rho = -0.42$ at $t - t_{\Delta M_{\rm BH}} = 300$ Myr is very strong.

We apply the same time series analysis to the covering fractions focusing on $C_{\rm C\,IV>13.5,100\,kpc}$ (solid blue line). The response to the

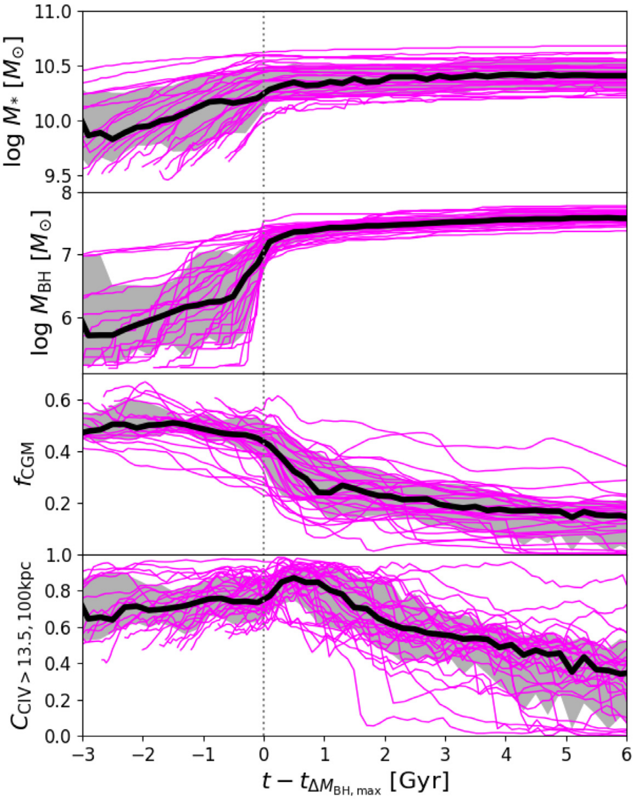

Figure 6. Similar to Fig. 5, but now shifted to the snipshot before the most rapid $M_{\rm BH}$ growth stage, where the BH increases by $\Delta M_{\rm BH} > 2\times10^6$ M$_\odot$ in an intersnipshot interval before $z=0.47$. Grey shading indicates $1-\sigma$ ranges. The $f_{\rm CGM}$ declines by 0.1 within 300 Myr after this growth stage, which is paired with a temporary increase in $C_{\rm C\,IV}$ followed by a several Gyr decline.

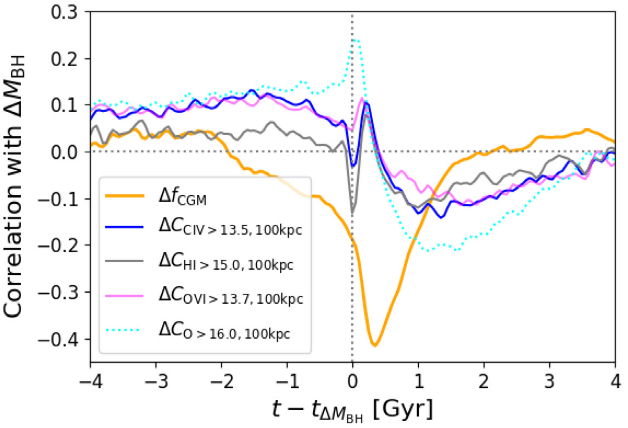

Figure 7. The relationships between the change in CGM quantities and BH growth as a function of time lag between BH growth at $t_{\Delta M_{\rm BH}}$ and the CGM quantity. Average Pearson correlation coefficients, ρ, are plotted for all haloes in the highest $E_{\rm BH}/\widetilde{E}^b_{\rm bind}$ quartile. The negative values of ρ plotted for $\Delta f_{\rm CGM}$ indicate CGM evacuation peaks 300 Myr after BH growth, and represents a direct indication that CGM gas fractions respond negatively to BH growth. CGM ion covering fractions decline as well, but with a longer lag of 0.5–2.5 Gyr after a BH growth episode, and actually increase in the first 100 Myr after BH growth due to the ejection of ISM gas. BH feedback initially drives metal enrichment as traced by the total oxygen covering fraction (dotted cyan line) before it declines after 400 Myr.

BH growth is more complicated. $C_{\rm C\,IV}$ was growing before $t_{\Delta M_{\rm BH}}$ indicating CGM metal enrichment, but does respond with a sharp drop at $t_{\Delta M_{\rm BH}}$. Yet, $C_{\rm C\,IV}$ jumps up at 200 Myr, before turning around and declining after 400 Myr. The greatest decline of $C_{\rm C\,IV}$ is between 500 Myr and 2.5 Gyr, showing a delayed response to the CGM ejection.

We also see the same general behaviour for $C_{\rm H\,I>15.0,100\,kpc}$ and $C_{\rm O\,VI>13.7,100\,kpc}$, but at differing strengths immediately after $t_{\Delta M_{\rm BH}}$. While it is very clear that $f_{\rm CGM}$ decreases in response to the BH, the three different ions have responses that depend on metallicity and ionization. To marginalize out ionization, we plot the total oxygen covering fraction above $N_{\rm O} > 10^{16.0}\,{\rm cm}^{-2}$, $C_{\rm O>16.0,100\,kpc}$ (dotted cyan) in Fig. 7, which shows a rapid increase around $t_{\Delta M_{\rm BH}}$ due to enrichment of the CGM by AGN feedback, which ejects metal-rich ISM into the CGM. The enrichment continues but at a sharply decreasing rate until $\Delta C_{\rm O}$ becomes negative after 300 Myr and remains negative for the next 3 Gyr. Hence, the decline in ions in this time interval is indicative of declining CGM metal content. Finally, we note that the dip at $t_{\Delta M_{\rm BH}}$ visible for the ion covering fraction is not present for $C_{\rm O}$, which indicates that the initial dip seen for the ions is due to AGN feedback changing the ionization state of the gas (likely via temporary heating of lower ions to higher states).

The trends here are general for all 246 galaxies of the secular sample, which shows the same trends in average correlation coefficients, but on average 2/3rd as strong when adding in the three quartiles of galaxies with lower $E_{\rm BH}/\widetilde{E}^{b}_{\rm bind}$.

6 GALAXY TRANSFORMATION AS A RESULT OF CGM EJECTION

The final goal of our exploration is to understand how the galaxy as a whole responds to CGM ejection driven by the black hole, since D19 demonstrated that SFR is highly correlated with $f_{\rm CGM}$ at fixed halo mass. We report SKIRT radiative transfer-processed colours (Trayford et al. 2017), because it furthers our goal of providing the most readily available observable proxies. The $u - r$ colours are observed for local galaxies in the SDSS.

We show our M^{*} sample by plotting $u - r$ as a function of $f_{\rm CGM}$ in Fig. 8, which shows just how dependent galaxy colour is on CGM baryon content. The lowest (highest) quartile of galaxies with $f_{\rm CGM} = 0.12\ (0.41)$ have median $u - r = 1.67\ (2.24)$. Galaxy colours depend on their CGM baryon content, which we have argued relies on the BH ejecting baryons. Hence, the content of the CGM out to at least 200 kpc is a predictor of galaxy colour according to EAGLE. The dark points with error bars are shown for the M^{*} sample ($M_{200} = 10^{12.0-12.3}\,{\rm M}_{\odot}$), but we also show the trend for all galaxies in the L^{*} sample in grey points and error bars to show the result is nearly same when considering all central galaxies with $M_{*} = 10^{10.2-10.7}\,{\rm M}_{\odot}$.

We argue that the result in Fig. 8 represents a new way to think about the origin of galaxy colours. Put another way, the bluest (reddest) quartile of L^{*} galaxies with $u - r = 1.59\ (2.28)$ have $f_{\rm CGM} = 0.34\ (0.13)$ according to EAGLE. For a more in-depth analysis of how red sequence galaxy colours arise in EAGLE, we refer the reader to Correa et al. (2019), who used the same snipshots to determine the time-scale and cause of galaxies crossing the green valley to the red sequence (see also Wright et al. 2019). They looked at both centrals and satellites, and integrated high-cadence colour and morphology tracking considering environmental effects, AGN feedback, and morphological transformation as pathways for all red sequence galaxies above $M_{*} = 10^{10}\,{\rm M}_{\odot}$. The most relevant result for us is their calculation of the time between the last time a red sequence galaxy entered the green valley and the peak black hole growth time-step, $t_{\Delta M_{\rm BH,max}}$. Their fig. 10 shows a practically instantaneous process (<1 Gyr centred on 0 Gyr) of a central galaxy entering the green valley in response to the largest BH growth phase in a galaxy's history. This agrees with our finding that the gas supply from the CGM is also disrupted nearly instantaneously through baryon clearing as shown in Figs 6 and 7.

We plot the median colour-M^{*} evolutionary paths of the four quartiles of the secular sample sorted by $E_{\rm BH}/\widetilde{E}^{b}_{\rm bind}$ in Fig. 9. The paths are fundamentally different between the lowest and highest $E_{\rm BH}/\widetilde{E}^{b}_{\rm bind}$ quartiles, for which we plot the individual $z = 0$ values in

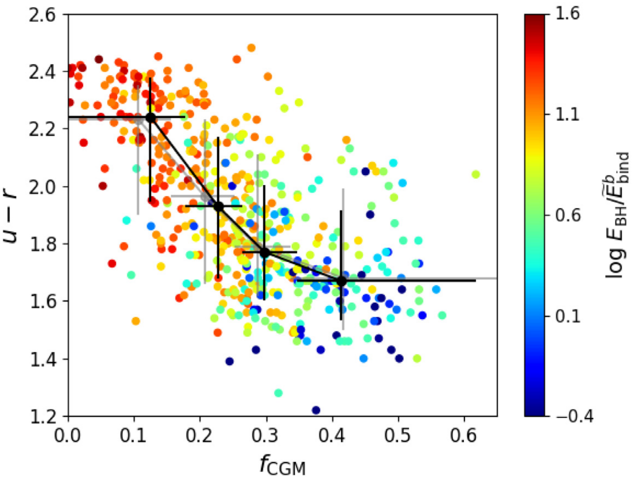

Figure 8. Galaxy colour plotted as a function of baryonic halo gas content with symbol colour indicating $E_{\rm BH}/\widetilde{E}^{b}_{\rm bind}$ for the M^{*} sample. Galaxy colour clearly depends on the baryonic content of the CGM, with the reddest galaxies all having very evacuated haloes compared to the bluest galaxies. Black points indicate running medians in quartiles of $u - r$ with ranges and $1 - \sigma$ spreads in $f_{\rm CGM}$. Grey points and bars show the same for the L^{*} sample.

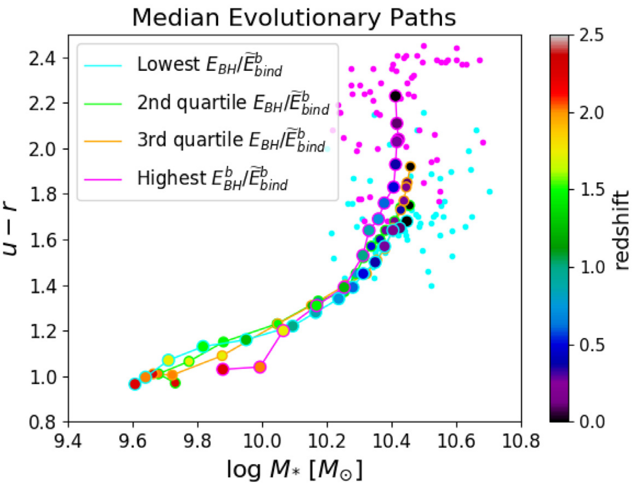

Figure 9. Median $u - r$ colour and median stellar mass evolution of galaxies in the secular sample divided into $E_{\rm BH}/\widetilde{E}^{b}_{\rm bind}$ quartiles. The three lower quartiles have similar evolutionary paths, but the highest quartile follows a divergent path that is redder since $z = 1$. The cyan (magenta) data points show individual $z = 0$ galaxies for the low-$E_{\rm BH}/\widetilde{E}^{b}_{\rm bind}$ (high-$E_{\rm BH}/\widetilde{E}^{b}_{\rm bind}$) quartile.

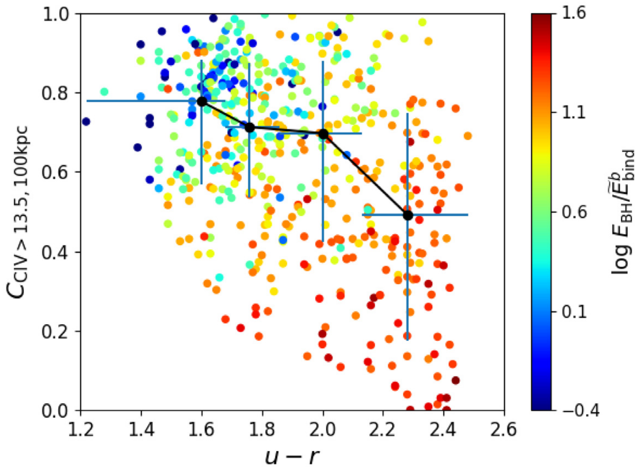

Figure 10. The C IV covering fraction plotted against galaxy colour and coloured by $E_{\rm BH}/\widetilde{E}^{b}_{\rm bind}$ for the M^{*} sample. Error bars use the same format as in Fig. 3. An observational version of this plot should be possible in the future, but the scatter is significantly reduced if $C_{\rm C\,IV}$ is plotted against $M_{\rm BH}$ instead (cf. Fig. 3).

cyan and magenta, respectively. First, the highest $E_{\rm BH}/\widetilde{E}^{b}_{\rm bind}$ haloes, which predominantly end up on the red sequence, show a divergence in colour from the other three paths going back to $z = 1$. These galaxies are predominantly morphologically elliptical (Correa et al. 2017), have their most intense black hole growth stages centred at $z \approx 1$ (Fig. 5), and form their stellar populations earlier at the centres of haloes that collapsed earlier (D19).

Secondly, the other three quartiles have comparatively similar median evolutionary paths resulting in colours that overlap more with the blue cloud. This is despite the fact that that each quartile of $E_{\rm BH}/\widetilde{E}^{b}_{\rm bind}$ has progressively lower values for $f_{\rm CGM}$. This indicates that secular AGN transformation to the red sequence requires a threshold energy of $E_{\rm BH}/\widetilde{E}^{b}_{\rm bind} \sim$ 10–15 for EAGLE MW-like haloes.

Finally, there exists significant scatter in $z = 0$ colours across the different quartiles, which is also apparent in Fig. 8. Even though $u - r$ colour is strongly correlated with BH feedback history, colours alone are not a direct predictor of the central black hole mass. We have not considered morphology, larger scale environment, nor major mergers for our galaxies, which are essential for describing all pathways of galaxy transformation. We are also avoiding the use of dust-free, intrinsic colours, which, while not directly observable, would reduce the scatter and produce clearer trends compared to our use of colours that include the effects of dust (Trayford et al. 2016).

Our approach is to provide the most direct observables to create a plot like Fig. 10 using observed galaxy-absorber pairs. Using the same format as Fig. 3, we show points coloured by $E_{\rm BH}/\widetilde{E}^{b}_{\rm bind}$ and medians with $1 - \sigma$ spreads on $C_{\rm C\,IV}$ and $u - r$ ranges for the M^{*} sample. These two galaxy-CGM observables shows a weaker correlation than a similar plot with $M_{\rm BH}$ replacing $u - r$ (Fig. 3). The point of showing this plot is that (1) it can be created by combining existing observations (Burchett et al. 2015) with future archival COS surveys (*CGM*^{2}, which would rely on using galaxies up to $z = 0.5$), and (2) we predict that obtaining $M_{\rm BH}$ will result in a tighter correlation than colour. We are hopeful that the predicted link between the BH and the CGM can be tested in the near future by collecting C IV sightlines around nearby L^{*} galaxies for which $M_{\rm BH}$ determinations exist.

7 DISCUSSION

7.1 How O VI traces the CGM

In Section 4 we argued that C IV provides the most promising observational proxy for $f_{\rm CGM}$. In this section we discuss O VI as a sensitive probe of CGM baryon content even if this ion is not currently locally available via COS. Considerable debate has emerged on the nature and origin of O VI in the COS-Haloes Survey after it was shown to be strong around blue, star-forming and weaker around red, passive $z \approx 0.2$ galaxies (Tumlinson et al. 2011). Oppenheimer et al. (2016) used EAGLE zooms to argue that O VI declined around passive galaxies, not due to baryon ejection, but instead owing to the ionization effect of these galaxies living in much more massive haloes ($M_{200} \sim 10^{13}\,{\rm M}_{\odot}$) with virial temperatures $> 10^{6}$ K. Nelson et al. (2018b) used the Illustris-TNG simulations with an updated BH feedback scheme (Weinberger et al. 2017) to show that O VI is reduced significantly by BH feedback in the M^{*} halo mass regime. Illustris-TNG also shows a stark decline in $f_{\rm CGM}$, falling from ≈0.6 to ≈0.2 for centrals with $M_{*} = 10^{10.3}$ to $10^{10.7}\,{\rm M}_{\odot}$ (Nelson et al. 2018b, their fig. 20, ii), which indicates baryon ejection by the BH.

Given that we are using the main EAGLE simulation, which shows the same trends as the zooms (Oppenheimer et al. 2016), we know that O VI declines for multiple reasons: BH feedback evacuating the halo (D19; this paper) at $M_{200} \sim 10^{12}{\rm M}_{\odot}$ and the virial temperature effect at higher halo masses (Oppenheimer et al. 2016). For EAGLE, median $f_{\rm CGM}$ increases monotonically with halo mass, while median $f_{\rm CGM}$ declines as a function of increasing halo mass over the M^{*} mass range in Illustris-TNG (Pillepich et al. 2018, their fig. 4, measured at a smaller radius). This indicates that BH ejection is not as aggressive in EAGLE, but it is still enough of a factor to reduce $f_{\rm CGM}$ significantly at fixed halo mass. A COS observational survey targeting C IV or O VI around star-forming and passive galaxies at fixed halo mass could be a better strategy to isolate the effect of BH evacuation of the CGM. It remains unclear if COS-Haloes passive galaxies live in similar mass haloes as their star-forming counterparts, but the passive galaxy stellar masses are mostly higher than $M_{*} = 10^{10.7}\,{\rm M}_{\odot}$ (Werk et al. 2012).

7.2 Consequences of black hole feedback efficiency

The energy efficiency of BH feedback has important consequences for a galaxy and its CGM. In EAGLE, the efficiency of the conversion of rest-mass energy of material accreting on to the BH to feedback energy is $\epsilon_{\rm BH} \equiv \epsilon_{r}\epsilon_{f} = 1.5$ per cent (Booth & Schaye 2009). The Illustris-TNG simulations use a two-mode BH feedback scheme where their thermal mode has $\epsilon_{\rm BH} = 2$ per cent and is used for high accretion rates, but their kinetic mode has $\epsilon_{\rm BH} = 20$ per cent and is used for low accretion rates (Weinberger et al. 2017). The kinetic mode operates primarily at later times and for later growth of the BH, and represents high efficiency jet feedback, which appears to be responsible for reducing O VI and $f_{\rm CGM}$ for passive M^{*} haloes in Illustris-TNG (Nelson et al. 2018b). The ROMULUS25 simulation uses a thermal BH feedback scheme with much lower efficiency, $\epsilon_{\rm BH} = 0.2$ per cent (Tremmel et al. 2017). Sanchez et al. (2019) demonstrated that the addition of BH feedback increases CGM metal enrichment, likely because it is not powerful enough to clear the CGM of baryons (their fig. 9), and may have more dynamical similarities to EAGLE's stellar feedback scheme.

Galaxy colours for both the EAGLE and Illustris-TNG 100 Mpc volumes show good agreement with observational data, but there are inherent differences. The EAGLE `SKIRT` dust-processed colours, which we use in our analysis, display a colour bimodality for L^* galaxies with slightly more blue peak galaxies than observed (Trayford et al. 2017, their fig. 7). The Illustris-TNG colours, applying 'resolved' dust attenuation based on the neutral gas and metal distributions within galaxies, display a colour bimodality with slightly more red peak galaxies for massive L^* galaxies than observed (Nelson et al. 2018a, their fig. 1). The red colours of Illustris-TNG L^* galaxies are likely more attributable to efficient BH feedback, while the red colours for EAGLE L^* galaxies are likely more influenced by dust effects. The feedback efficiency of the BH central engine appears to be linked to both the CGM gas content and the galaxy's stellar assembly and colour when comparing EAGLE and Illustris-TNG, which is the subject of Davies et al. (2019b). The ROMULUS25 volume is far smaller and the passive galaxy fraction is not defined in the same way, but Tremmel et al. (2019) shows L^* field galaxies have a quenched fraction between ~ 25 and 45 per cent (their fig. 14). Combined with Sanchez et al. (2019), this suggests that other mechanisms besides baryon clearing can cause their simulated L^* centrals to appear quenched.

7.3 The Milky Way CGM–black hole connection

The most recent estimates of the MW halo mass are closer to $M_{200} = 10^{12.0}\,\mathrm{M}_{\odot}$ (e.g. Eadie & Jurić 2019), though we consider the range of possibilities to be $10^{12.0}-10^{12.3}\,\mathrm{M}_{\odot}$ (e.g. Battaglia et al. 2005). Sgr A* has a mass of $4 \times 10^6\,\mathrm{M}_{\odot}$ (Boehle et al. 2016), which puts our galaxy below $M_{\rm BH}/M_{200} < 10^{-5}$ and suggests it is most similar to galaxies in the lowest $E_{\rm BH}/\widetilde{E}^{b}_{\rm bind}$ quartile. We use the Bregman et al. (2018) estimates for the total CGM mass, and assume their values of $M_{\rm CGM,T<10^5K} = 10^{10}\mathrm{M}_{\odot}$ and $M_{\rm CGM,T\geq 10^5K} = 6 \times 10^{10}\,\mathrm{M}_{\odot}$, and plot the MW's $f_{\rm CGM}$ for four assumed halo masses in Fig. 1. The MW's gaseous halo appears to agree with the EAGLE model, especially if its M_{200} is indeed closer to $10^{12.0}$ than $10^{12.3}\,\mathrm{M}_{\odot}$. The MW contains an undermassive BH and a higher $f_{\rm CGM}$ compared to average MW-mass haloes. Further constraints on the MW CGM mass, especially its hot component at larger radii, will allow more accurate explorations of our halo's BH–CGM link. While halo gas fractions of clusters appear overestimated by the EAGLE model (Barnes et al. 2017, C-EAGLE), the $f_{\rm CGM}$ gas fractions of MW-mass haloes are observationally unconstrained.

Our results suggest that the MW may be on the precipice of an epoch of rapid BH growth and CGM evacuation. Using the sequence that Bower et al. (2017) derived from EAGLE, the growth of the hot halo leads to a reduction in the efficiency of feedback from star formation. Ineffective stellar feedback results in gas collecting near the galaxy centre, leading to rapid BH growth and AGN feedback (see also Dubois et al. 2015; Anglés-Alcázar et al. 2017), which we argue can eject a large fraction of the baryons from our halo. However, it must be realized that similar mass haloes with massive BHs underwent the stage of rapid BH growth at much higher redshift, and that the MW halo is not interchangeable with a halo of the same mass hosting a passive galaxy. D19 showed that high-$M_{\rm BH}$ haloes had earlier formation times than low-$M_{\rm BH}$ haloes. This is also interesting for the MW, because metal abundance patterns of the MW disc (Mackereth et al. 2018) and the MW globular cluster age-metallicity distribution (Kruijssen et al. 2018) suggest an earlier formation history than typical disc galaxies occupying $\sim 10^{12}\,\mathrm{M}_{\odot}$ haloes. Combined with the later formation times implied by its undermassive BH, the MW system could be atypical.

8 SUMMARY

We analyse the largest EAGLE simulation to understand how the baryonic content of MW-mass galaxy haloes react to the growth of their central supermassive black holes and how the resulting evolution transforms the galaxies. We argue that it is necessary to observe the circumgalactic medium to attempt to understand the roles of BH growth and AGN feedback in galaxy transformation. Our investigation leverages the high-cadence tracking of a large sample of simulated galaxies to catch the act of 'baryon lifting', where the BH feedback energy can eject most of the circumgalactic baryons from the halo and transform the galaxy across the green valley to the red sequence. We argue that a key physical quantity is the time integral of the total energy released by the BH divided by an analytical estimate of the binding energy of the gaseous halo ($E_{\rm BH}/\widetilde{E}^{b}_{\rm bind}$). We attempt to relate these physical characteristics to accessible observational proxies of (1) the cumulative BH feedback energy, through $M_{\rm BH}$, (2) the gaseous content of the CGM, through ion column densities and covering fractions, and (3) the star formation history of the galaxy, through $u - r$ colours.

This work is an extension of Davies et al. (2019a), who identified $M_{\rm BH}$ as being highly anticorrelated with the halo gas fractions, $f_{\rm CGM}$, in EAGLE. Here, we mainly focus on present-day L^*-mass galaxies ($M_* = 10^{10.2-10.7}\,\mathrm{M}_{\odot}$) residing in MW-mass haloes ($M_{200} = 10^{12.0-12.3}\,\mathrm{M}_{\odot}$) that show a great diversity not only in galaxy colours, but also in $M_{\rm BH}$ and $f_{\rm CGM}$. The main results of our investigation connecting the scales of BHs, galaxies, and the CGM are as follows:

(i) While $f_{\rm CGM}$ is strongly anticorrelated with $M_{\rm BH}$ at a given halo mass, the anticorrelation with $E_{\rm BH}/\widetilde{E}^{b}_{\rm bind}$ is more essential over varied halo masses that $M_* = 10^{10.2-10.7}\,\mathrm{M}_{\odot}$ galaxies occupy. The median value of $f_{\rm CGM}$ is 0.37 (0.13) in the lowest (highest) quartile of $E_{\rm BH}/\widetilde{E}^{b}_{\rm bind}$, which has a median value of $E_{\rm BH}/\widetilde{E}^{b}_{\rm bind} = 1.6$ (18), (Section 3, Fig. 2).

(ii) We explore covering fractions for several ions observable (by COS), including H I, C IV, and O VI, and argue that the $N_{\rm C\,IV} > 10^{13.5}\,\mathrm{cm}^{-2}$ covering fraction within 100 kpc of the galaxy, $C_{\rm C\,IV}$, is most easily obtainable for local galaxies where BH mass estimates are most readily available. $C_{\rm C\,IV}$ mirrors the trend of $f_{\rm CGM}$ and declines from 0.79 to 0.43 from the lowest to the highest $M_{\rm BH}$ quartile. O VI is also an effective $f_{\rm CGM}$ proxy, but is not locally available with COS (Section 4, Fig. 3).

(iii) High-cadence tracking of a subset of our galaxies indicates a causal link between $M_{\rm BH}$ and $f_{\rm CGM}$. $f_{\rm CGM}$ responds to BH growth on a cosmologically very short, $<$100 Myr, time-scale. Ion covering fractions take longer to decline in response to episodes of BH growth (0.5–2.5 Gyr), which is in part due to AGN-driven metal transport from the ISM to the CGM. The strong anticorrelation between the $M_{\rm BH}$ and $f_{\rm CGM}$ originates from BH feedback episodes concentrated in time, usually at $z \gtrsim 1$ (Section 5, Figs 5, 6, 7).

(iv) The $u - r$ colours, calculated using the `SKIRT` radiative transfer dust-reddening model, have values of $2.23^{+0.15}_{-0.38}$ and $1.68^{+0.20}_{-0.14}$ for the highest and lowest $E_{\rm BH}/\widetilde{E}^{b}_{\rm bind}$ quartiles. Hence, haloes having undergone significant secular BH growth are more likely to be red sequence galaxies, while their low-$M_{\rm BH}$ counterparts likely remain in the blue cloud. However, the significant dispersion in $u - r$ values indicates that $E_{\rm BH}/\widetilde{E}^{b}_{\rm bind}$ alone is not a good predictor of colour (Section 6, Figs 8, 9, 10).

(v) The MW itself has a low-$E_{\rm BH}/\widetilde{E}^{b}_{\rm bind}$ ratio, calculated using the mass of Sgr A*, which would indicate that it should have a high $f_{\rm CGM}$ for its halo mass. Estimates for the observed CGM mass of the MW (e.g. Bregman et al. 2018) suggest that it retains more gas than the average halo if its M_{200} is $\approx 10^{12.0}$ M$_\odot$, although these CGM mass estimates are currently highly unconstrained (Section 7.3, Fig. 1).

(vi) Although the time-integrated stellar feedback energy released is greater than the BH feedback released in most EAGLE MW-like haloes, the more gradual release of stellar energy to the CGM does not clear the halo, but maintains a cycle of accretion, feedback, and re-accretion as the galaxy evolves along the star-forming sequence. The energy release due to rapid growth of the BH can disrupt and fundamentally change the cycle of baryons between the CGM and galaxies, leaving lasting impacts on both.

We put forth that a fundamental pathway for secular galaxy transformation involves a three-step sequence: (1) the formation of a hot halo, (2) the rapid growth of the BH, and (3) the lifting by AGN feedback of the baryonic halo curtailing the supply of fuel for star formation. The first two of these processes were linked in EAGLE by Bower et al. (2017), who argued that the hot halo prevents effective SF feedback from buoyantly rising into the CGM, leading to increased accretion on to and rapid growth of the central BH. Davies et al. (2019a) revealed the inverse correlation between $M_{\rm BH}$ and $f_{\rm CGM}$ in EAGLE, suggesting a causal link between the BH and the removal of a significant portion of the gas from the halo, which reduces CGM accretion and galactic star formation. We uncover this causal link in a set of galaxies that rapidly grow their BHs, eject baryons from their haloes, and transform their colours.

Our analysis contends that the efficiency with which a BH couples its feedback energy to the CGM is essential for understanding the process of secular galaxy transformation. Davies et al. (2019b) further demonstrates that the quenching and morphological transformation of galaxies is facilitated by feedback-driven CGM expulsion for galaxy haloes in general in EAGLE *and* Illustris-TNG. We argue the relationship between a galaxy's stellar assembly, its halo gas supply, and its central BH should be a focus of CGM-oriented studies going forward. We emphasize the need for observational campaigns targeting local galaxies, where non-AGN BH masses and dynamical halo masses are, or will become, available.

ACKNOWLEDGEMENTS

The authors acknowledge the referee's thorough review of our manuscript, which enhanced and clarified this work. The authors would like to thank Akos Bogdan, Lars Hernquist, Ian McCarthy, Dylan Nelson, Erica Nelson, Nicole Sanchez, John Stocke, Michael Tremmel, and Rainer Weinberger for stimulating conversations and exchanges that contributed to this manuscript. Support for BDO was provided through the NASA ATP grant NNX16AB31G and NASA *Hubble* grant *HST*-AR-14308. JJD acknowledges an STFC doctoral studentship. RAC is a Royal Society University Research Fellow. JKW acknowledges support from a 2018 Sloan Foundation Fellowship. JS acknowledges support from Vici grant 639.043.409 from the Netherlands Organisation for Scientific Research (NWO). The study made use of high performance computing facilities at Liverpool John Moores University, partly funded by the Royal Society and LJMU's Faculty of Engineering and Technology, and the DiRAC Data Centric system at Durham University, managed by the Institute for Computational Cosmology on behalf of the STFC DiRAC HPC Facility (http://www.dirac.ac.uk). This equipment was funded by BEIS capital funding via STFC capital grants ST/K00042X/1, ST/P002293/1, ST/R002371/1, and ST/S002502/1,Durham University and STFC operations grant ST/R000832/1. DiRAC is part of the National e-Infrastructure.

REFERENCES

Anglés-Alcázar D., Faucher-Giguère C.-A., Quataert E., Hopkins P. F., Feldmann R., Torrey P., Wetzel A., Kereš D., 2017, MNRAS, 472, L109
Balogh M. L., Pearce F. R., Bower R. G., Kay S. T., 2001, MNRAS, 326, 1228
Barnes D. J. et al., 2017, MNRAS, 471, 1088
Battaglia G. et al., 2005, MNRAS, 364, 433
Behroozi P. S., Wechsler R. H., Conroy C., 2013, ApJ, 770, 57
Berg T. A. M., Ellison S. L., Tumlinson J., Oppenheimer B. D., Horton R., Bordoloi R., Schaye J., 2018, MNRAS, 478, 3890
Boehle A. et al., 2016, ApJ, 830, 17
Bogdán Á., Forman W. R., Kraft R. P., Jones C., 2013, ApJ, 772, 97
Bondi H., Hoyle F., 1944, MNRAS, 104, 273
Booth C. M., Schaye J., 2009, MNRAS, 398, 53
Bordoloi R. et al., 2014, ApJ, 796, 136
Borthakur S. et al., 2015, ApJ, 813, 46
Bower R. G., Benson A. J., Malbon R., Helly J. C., Frenk C. S., Baugh C. M., Cole S., Lacey C. G., 2006, MNRAS, 370, 645
Bower R. G., Schaye J., Frenk C. S., Theuns T., Schaller M., Crain R. A., McAlpine S., 2017, MNRAS, 465, 32
Bregman J. N., Anderson M. E., Miller M. J., Hodges-Kluck E., Dai X., Li J.-T., Li Y., Qu Z., 2018, ApJ, 862, 3
Burchett J. N. et al., 2015, ApJ, 815, 91
Burchett J. N. et al., 2016, ApJ, 832, 124
Camps P., Baes M., 2015, Astron. Comput., 9, 20
Camps P. et al., 2018, ApJS, 234, 20
Chen H.-W., Lanzetta K. M., Webb J. K., 2001, ApJ, 556, 158
Cooksey K. L., Thom C., Prochaska J. X., Chen H.-W., 2010, ApJ, 708, 868
Correa C. A., Schaye J., Clauwens B., Bower R. G., Crain R. A., Schaller M., Theuns T., Thob A. C. R., 2017, MNRAS, 472, L45
Correa C. A., Schaye J., Trayford J. W., 2019, MNRAS, 484, 4401
Crain R. A. et al., 2015, MNRAS, 450, 1937
Croton D. J. et al., 2006, MNRAS, 365, 11
Dalla Vecchia C., Schaye J., 2012, MNRAS, 426, 140
Danforth C. W. et al., 2016, ApJ, 817, 111
Davé R., Oppenheimer B. D., 2007, MNRAS, 374, 427
Davé R., Thompson R., Hopkins P. F., 2016, MNRAS, 462, 3265
Davies J. J., Crain R. A., McCarthy I. G., Oppenheimer B. D., Schaye J., Schaller M., McAlpine S., 2019a, MNRAS, 485, 3783(D19)
Davies J. J., Crain R. A., Oppenheimer B. D., Schaye J., 2019b, preprint (arXiv:1908.11380)
Dubois Y., Volonteri M., Silk J., Devriendt J., Slyz A., Teyssier R., 2015, MNRAS, 452, 1502
Dubois Y., Peirani S., Pichon C., Devriendt J., Gavazzi R., Welker C., Volonteri M., 2016, MNRAS, 463, 3948
Eadie G., Jurić M., 2019, ApJ, 875, 159
Ford A. B., Oppenheimer B. D., Davé R., Katz N., Kollmeier J. A., Weinberg D. H., 2013, MNRAS, 432, 89
Ford A. B., Davé R., Oppenheimer B. D., Katz N., Kollmeier J. A., Thompson R., Weinberg D. H., 2014, MNRAS, 444, 1260
Greco J. P., Hill J. C., Spergel D. N., Battaglia N., 2015, ApJ, 808, 151
Haardt F., Madau P., 2001, in Neumann D. M., Tran J. T. V., eds, Recent results of XMM-Newton and Chandra, XXXVIth Rencontres de Moriond, XXIst Moriond Astrophysics Meeting, March 10-17, 2001 Savoie, France, p. 64
Henriques B. M. B., White S. D. M., Thomas P. A., Angulo R., Guo Q., Lemson G., Springel V., Overzier R., 2015, MNRAS, 451, 2663
Hopkins P. F., 2013, MNRAS, 428, 2840
Keeney B. A. et al., 2017, ApJS, 230, 6
Kereš D., Katz N., Weinberg D. H., Davé R., 2005, MNRAS, 363, 2
Kormendy J., Ho L. C., 2013, ARA&A, 51, 511
Kruijssen J. M. D., Pfeffer J. L., Reina-Campos M., Crain R. A., Bastian N., 2018, MNRAS, 1, 22

Liang C. J., Chen H.-W., 2014, MNRAS, 445, 2061
Li J.-T., Bregman J. N., Wang Q. D., Crain R. A., Anderson M. E., Zhang S., 2017, ApJS, 233, 20
Mackereth J. T., Crain R. A., Schiavon R. P., Schaye J., Theuns T., Schaller M., 2018, MNRAS, 477, 5072
McAlpine S. et al., 2016, Astron. Comput., 15, 72
McMillan P. J., 2011, MNRAS, 414, 2446
Moster B. P., Naab T., White S. D. M., 2013, MNRAS, 428, 3121
Moustakas J. et al., 2013, ApJ, 767, 50
Nelson D. et al., 2018a, MNRAS, 475, 624
Nelson D. et al., 2018b, MNRAS, 477, 450
Oppenheimer B. D., 2018, MNRAS, 480, 2963
Oppenheimer B. D., Davé R., 2006, MNRAS, 373, 1265
Oppenheimer B. D., Davé R., Kereš D., Fardal M., Katz N., Kollmeier J. A., Weinberg D. H., 2010, MNRAS, 406, 2325
Oppenheimer B. D. et al., 2016, MNRAS, 460, 2157
Oppenheimer B. D., Schaye J., Crain R. A., Werk J. K., Richings A. J., 2018, MNRAS, 481, 835
Pillepich A. et al., 2018, MNRAS, 473, 4077
Planck Collaboration XI, 2013, A&A, 557, A52
Prochaska J. X. et al., 2017, ApJ, 837, 169
Rahmati A., Pawlik A. H., Raičević M., Schaye J., 2013, MNRAS, 430, 2427
Rahmati A., Schaye J., Crain R. A., Oppenheimer B. D., Schaller M., Theuns T., 2016, MNRAS, 459, 310
Rees M. J., Ostriker J. P., 1977, MNRAS, 179, 541
Rosas-Guevara Y., Bower R. G., Schaye J., McAlpine S., Dalla Vecchia C., Frenk C. S., Schaller M., Theuns T., 2016, MNRAS, 462, 190
Rosas-Guevara Y. M. et al., 2015, MNRAS, 454, 1038
Sanchez N. N., Werk J. K., Tremmel M., Pontzen A., Christensen C., Quinn T., Cruz A., 2019, ApJ, 882, 8
Schaye J., Dalla Vecchia C., 2008, MNRAS, 383, 1210
Schaye J., Aguirre A., Kim T.-S., Theuns T., Rauch M., Sargent W. L. W., 2003, ApJ, 596, 768
Schaye J. et al., 2010, MNRAS, 402, 1536
Schaye J. et al., 2015, MNRAS, 446, 521
Sijacki D., Springel V., Di Matteo T., Hernquist L., 2007, MNRAS, 380, 877
Silk J., 1977, ApJ, 211, 638
Somerville R. S., Hopkins P. F., Cox T. J., Robertson B. E., Hernquist L., 2008, MNRAS, 391, 481
Springel V., 2005, MNRAS, 364, 1105
Springel V., Hernquist L., 2003, MNRAS, 339, 312
Springel V., Di Matteo T., Hernquist L., 2005, MNRAS, 361, 776
Stocke J. T., Keeney B. A., Danforth C. W., Shull J. M., Froning C. S., Green J. C., Penton S. V., Savage B. D., 2013, ApJ, 763, 148
Trayford J. W., Theuns T., Bower R. G., Crain R. A., Lagos C. d. P., Schaller M., Schaye J., 2016, MNRAS, 460, 3925
Trayford J. W. et al., 2017, MNRAS, 470, 771
Tremmel M., Karcher M., Governato F., Volonteri M., Quinn T. R., Pontzen A., Anderson L., Bellovary J., 2017, MNRAS, 470, 1121
Tremmel M. et al., 2019, MNRAS, 483, 3336
Tumlinson J. et al., 2011, Science, 334, 948
Tumlinson J. et al., 2013, ApJ, 777, 59
Tumlinson J., Peeples M. S., Werk J. K., 2017, ARA&A, 55, 389
Turner M. L., Schaye J., Crain R. A., Rudie G., Steidel C. C., Strom A., Theuns T., 2017, MNRAS, 471, 690
Weinberger R. et al., 2017, MNRAS, 465, 3291
Werk J. K., Prochaska J. X., Thom C., Tumlinson J., Tripp T. M., O'Meara J. M., Meiring J. D., 2012, ApJS, 198, 3
Werk J. K. et al., 2014, ApJ, 792, 8
White S. D. M., Frenk C. S., 1991, ApJ, 379, 52
White S. D. M., Rees M. J., 1978, MNRAS, 183, 341
Wiersma R. P. C., Schaye J., Smith B. D., 2009a, MNRAS, 393, 99
Wiersma R. P. C., Schaye J., Theuns T., Dalla Vecchia C., Tornatore L., 2009b, MNRAS, 399, 574
Wright R. J., Lagos C. d. P., Davies L. J. M., Power C., Trayford J. W., Wong O. I., 2019, MNRAS, 487, 3740

This paper has been typeset from a TEX/LATEX file prepared by the author.